Journal of Structural Geology 180 (2024) 105078

Contents lists available at ScienceDirect

Journal of Structural Geology

journal homepage: www.elsevier.com/locate/jsg

The influence of the geometry of salt detachments on thrust salient development: An analogue modelling approach based on the South-Central Pyrenean thrust salient

Josep A. Muñoz *, Oriol Ferrer, Oscar Gratacós, Eduard Roca

Departament de Dinàmica de la Terra i de L'Oceà, Facultat de Ciències de la Terra, Institut de Recerca Geomodels, Universitat de Barcelona (UB), C/ Martí i franquès s/n, Zona universitària de Pedralbes, 08028, Barcelona, Spain

ARTICLE INFO

Keywords:
Analogue modelling
Oblique structures
South-Central Pyrenees
Salt-detached fold-and-thrust belts
Thrust salients

ABSTRACT

Inspired by the structural evolution of the South-Central Pyrenean Thrust Salient we have designed an experimental program to investigate the role of the geometry of viscous detachments on the formation of thrust salients. The precontractional wedge geometry of the salt overburden facilitates propagation of the deformation front to the forward edge of the viscous detachment. As deformation progresses, interaction between structures formed above the viscous detachment and the adjacent frictional detachment mostly depends on the angles of the lateral edges of the weak layer with respect to the shortening direction. The orientation of the oblique structures defining thrust salients does not generally mimic the edges of the viscous detachment. They can even form at a high angle to the shortening direction if active structures in the frictional and viscous detachments connect along-strike. Thrust wedges above frictional and viscous detachments show different kinematic evolution. During the late stages of deformation frictional wedges propagate forward whereas viscous wedges deform internally by break-back thrust sequences. Both wedges show along-strike differences of the surface taper that have an impact on the evolution of the topography and related synorogenic sediment dispersal. Experimental results are consistent with the structural evolution and tectono-sedimentary relationships observed in the South-Central Pyrenees.

1. Introduction

Most fold-and-thrust belts involving salt layers exhibit curved structures in the form of thrust salients (curved structures convex toward the transport direction) and recesses (curves concave toward the direction of transport) (Marshak, 2004). Examples include the Zagros fold-and-thrust belt (Sepehr and Cosgrove, 2004; Callot et al., 2007), the Sierra Madre Oriental (Fischer and Jackson, 1999), the Jura Mountains (Becker, 2000; Smeraglia et al., 2021), the South-Western Alps (Célini et al., 2020) and the Pyrenees (Muñoz et al., 2018; Cámara, 2020). Deciphering the origin of thrust salients in these fold-and-thrust belts relies on interpreting the oblique and lateral structures forming these thrust salients. They have been interpreted as related either to oblique or transverse basement-involved structural features beneath the salt layer (Sepehr and Cosgrove, 2004) or structures involving only the suprasalt succession developed during contractional deformation. Suprasalt oblique structures may form either by displacement gradient above an unevenly distributed salt layer (Bahroudi and Koyi, 2003; Muñoz et al., 2013, 2018), or by the reactivation of salt structures (Rowan and Vendeville, 2006; Callot et al., 2012; Duffy et al., 2018; Santolaria et al., 2021).

Curved orogens or fold-and-thrust systems have been classified into primary, progressive, and secondary based on factors such as the timing between thrusting and rotation, and the presence or absence of vertical axis rotation (Weil and Sussman, 2004; Weil et al., 2010). Primary arcuate fold-and-thrust systems are initially formed with a curved geometry and do not exhibit any vertical axis rotation. These systems typically occur due to the inversion of faults or basins showing along-strike changes in orientation. On the other end of the spectrum, secondary curved systems or oroclines arise from the bending of initially linear structures around a vertical axis (Marshak, 2004). In progressive curved systems, the strike of structures undergoes gradual changes during deformation. In these systems, rotation and thrusting take place simultaneously (Weil et al., 2010).

* Corresponding author.
E-mail addresses: jamunoz@ub.edu (J.A. Muñoz), oferrer@ub.edu (O. Ferrer), ogratacos@ub.edu (O. Gratacós), eduardroca@ub.edu (E. Roca).

https://doi.org/10.1016/j.jsg.2024.105078
Received 15 October 2023; Received in revised form 26 January 2024; Accepted 1 February 2024
Available online 11 February 2024

The southern Pyrenees show numerous salients and recesses, but the most prominent thrust salient is in the South-Central Pyrenees (Fig. 1). This feature has attracted the attention of structural geologists since the first half of the last century (Misch, 1934). It was interpreted as a primary curvature inherited from the geometry of Mesozoic Basins and named the South-Pyrenean Central Unit (Séguret, 1972). However, paleomagnetic data acquired after the 1990's have demonstrated that most of the oblique structures have experienced vertical-axis rotations (Dinarès et al., 1992; Sussman et al., 2004; Mochales et al., 2012; Rodriguez-Pintó et al., 2016) suggesting that the South-Central

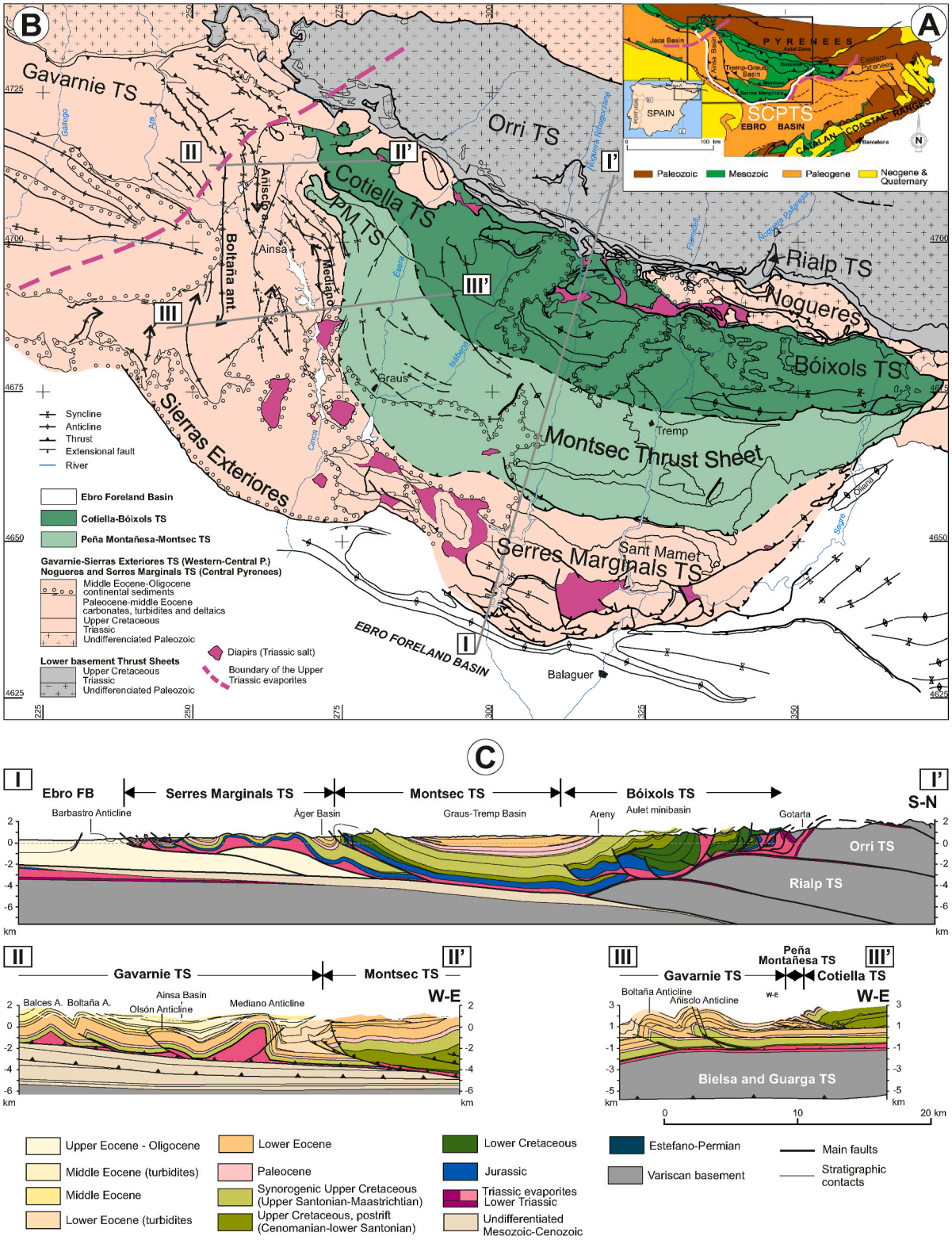

Fig. 1. A) Location of the study area. B) Structural map of the South-Central Pyrenean Thrust Salient. C) Representative cross-sections across the western edge and central part of the South-Central Pyrenean Thrust Salient. FB: foreland basin; PMTS: Peña Montañesa Thrust Sheet; SCPTS: South-Central Pyrenean Thrust Salient; TS: thrust sheet. Modified from Muñoz et al. (2013, 2018).

Pyrenean Thrust Salient is a progressive curvature formed by thrust displacement gradient (Oliva-Urcía and Pueyo, 2007; Muñoz et al., 2013).

Several analogue modelling studies have focused on the formation and evolution of thrust salients in salt-detached fold-and-thrust belts, addressing the main factors controlling them as well as the structures that develop at the transition from frictional to viscous detachments (see Santolaria et al., 2024, for an extensive review). These studies have demonstrated that an uneven distribution of the weak layer at the bottom of the deformed wedge results in the development of thrust salients and recesses, as deformation propagates farther and faster into the foreland above a ductile detachment (Cotton and Koyi, 2000; Costa and Vendeville, 2002; Bahroudi and Koyi, 2003; Vidal-Royo et al., 2009; Li and Mitra, 2017; Borderie et al., 2018; Pla et al., 2019). Such differences in the propagation rate between the adjacent frictional and viscous detachments result in thrust wedges with different surface taper, with that above the viscous detachment being wider and showing a smaller taper angle, as predicted by Coulomb taper theory (Davis et al., 1983; Davis and Engelder, 1985). Most experimental studies also conclude that deformation along the lateral edges of the viscous detachment is characterized by either an array of oblique contractional structures or by strike-slip faults parallel to the shortening direction. Both would form parallel to and along the lateral edges of the silicone polygons by their development as transpressional or strike-slip structures. Models including oblique orientations of the lateral terminations of the viscous detachment have shown the development of oblique thrusts following the initial orientation of the silicone edges (Santolaria et al., 2024). Thus, structures developed in a contractionally deformed sand package above an unevenly distributed viscous detachment would mimic the initial geometry of this detachment. Such a model has been applied to the interpretation of salt-detached fold-and-thrust belts (see references above).

However, most experiments have been performed with a similar setup characterized by a parallel, layer-cake dry silica sand package above a rectangular silicone prismatic body with lateral edges parallel to the shortening direction. Very few experiments explore the influence of an oblique orientation of the viscous silicone lateral edges in the formation of oblique structures in the transitional domains with the frictional detachment (Lickorish et al., 2002; Luján et al., 2003) or explore setups in which silicone and the overlying sand layers do not have a prismatic shape (Pla et al., 2019). Storti et al. (2007) explored the effect on the structural architecture of an along-strike taper geometry above a viscous detachment with a rectangular shape.

Our study builds on previous analogue modelling programs but introduces differences in the setup with respect to published work. The design of our experiments has been inspired by the observed structures of the South-Central Pyrenean Thrust Salient and the restored distribution of the salt layer at the bottom of the deformed succession (Muñoz et al., 2013). In addition, shortening has been transmitted to the sand wedge using the "subduction model" configuration of Graveleau et al. (2012). With this new approach we bring new ideas, and question some of the published conclusions about the formation and kinematics of thrust salient structures in salt-detached fold-and-thrust belts.

2. Geological setting

The Pyrenees are a collisional mountain range between the Iberian and European plates that formed from Late Cretaceous to Miocene times. Mountain building occurred as the Iberian plate was subducted beneath the European one, and the previous rifted margin that developed in the Bay of Biscay and Pyrenean domain was incorporated into the mountain belt (Muñoz, 1992; Teixell et al., 2018). The structural style of the chain, as well as its along-strike changes, mostly resulted from the inversion of the Late Jurassic-Early Cretaceous rift system (Manatschal et al., 2021). However, the distribution of Upper Triassic salt at the bottom of the Mesozoic sedimentary package also played a major role, even at the crustal scale (Beaumont et al., 2000; Jourdon et al., 2020). The Upper Triassic salt is unevenly distributed along the Pyrenean orogen due to the inherited Triassic extensional faults and subsequent erosion (López-Gómez et al., 2019). In areas where the salt is present, deformation of the overlying sedimentary succession has been decoupled from that of the basement, resulting in a largely thin-skinned structural style, such as in the Basque-Cantabrian Pyrenees and the Central Pyrenees. In contrast, inversion of the Late Jurassic-Early Cretaceous extensional fault system and the inherited Variscan structural features have promoted basement involvement in areas where the Triassic salt is absent, such as the Cantabrian mountains and the Eastern Pyrenees (Alonso et al., 1996; Jammes et al., 2014).

This paper focuses on the South-Central Pyrenees, characterized by the most prominent thrust salient in the Pyrenean fold-and-thrust belt (Fig. 1). It was previously described as the South Pyrenean Central Unit (Séguret, 1972), but we prefer to use the term South-Central Pyrenean Thrust Salient because it does not form a single structural unit, like a primary arch (Muñoz et al., 2013).

The South-Central Pyrenean Thrust Salient involves the main structural units of the southern Pyrenees. It shows an asymmetric geometry in map view and a general westward plunge of the main folds (Fig. 1). The western edge is characterized by a system of N–S trending folds, mainly developed in the eastern part of the Gavarnie thrust sheet and in its frontal part at the Sierras Exteriores thrust front. These N–S trending structures are also referred to as the Ainsa Oblique Zone (Muñoz et al., 2013). The eastern part of the South-Central Pyrenean Thrust Salient consists of NE-SW trending oblique structures that tend to merge eastwards. East of the thrust salient, the Eastern Pyrenees are narrower, and the southern Pyrenean thrust sheets are piled one on top of the other (Fig. 1). There, the Upper Triassic salt is absent, and the Upper Cretaceous to Paleocene sediments rest directly above the basement rocks (Muñoz et al., 1986; Vergés, 1993). The salt-decoupled Mesozoic-Paleogene succession of the South-Central Pyrenean Thrust Salient has been involved in three main thrust sheets, which from North to South are: Cotiella-Bóixols, Peña Montañesa-Montsec, and Serres Marginals (Fig. 1). The Mesozoic succession thins southward from the Cotiella-Bóixols Thrust Sheet, where it can be as thick as 6–7 km, to the frontal parts of the Serres Marginals Thrust Sheet where the total thickness can be only a few tens of meters (Fig. 1C, section I-I'; Muñoz et al., 2018). These thrust sheets initially developed following a forward propagating thrust sequence from Late Cretaceous to late Eocene times, but younger latest Eocene-early Miocene break-back thrust sequences, as well as out-of-sequence thrusts reactivating former ones, are prominent in the Serres Marginals and Montsec Thrust Sheets, mainly in their central and eastern areas (Vergés and Muñoz, 1990; Muñoz, 2002).

The Cotiella-Bóixols Thrust Sheet resulted from the inversion of the Lower Cretaceous extensional basins at the southern margin of the Pyrenean rift system. It involved thick syn-rift successions (Berastegui et al., 1990; Mencos et al., 2015), and Upper Cretaceous postrift sediments. Sediment accommodation was controlled by a combination of extension and salt evacuation (McClay et al., 2004; López-Mir et al., 2014; Saura et al., 2016). The Peña Montañesa-Montsec Thrust Sheet involves the northern part of the Upper Cretaceous foreland basin characterized by a strongly subsident turbiditic trough at the footwall of the Cotiella and Bóixols thrusts and a coeval southward-retreating carbonate platform (Martín-Chivelet, et al., 2019). The Peña Montañesa-Montsec Thrust Sheet was emplaced from the Paleocene to the early Eocene, as recorded by continental to shallow marine sediments deposited in its footwall (Ager Basin) as well as in the Graus-Tremp piggy-back basin (Fig. 1C). The lower-middle Eocene sediments of these basins grade westward into the slope sediments of the Ainsa Basin in the footwall of the Montsec thrust across the oblique structures at its western edge (Mutti et al., 1988). The folds of the Ainsa Oblique Zone controlled the sedimentary infilling of the Ainsa Basin and its transition to the Jaca Basin (Fernández et al., 2012). To the north, these folds have a fault-propagation fold geometry, with fold axes that trend NW-SE to

N–S and are subhorizontal or southward plunging. Further south, in contrast, the structural style is characterized by N–S trending detachment folds involving a Triassic salt succession. They are, from east to west, the Mediano, Olsón, Boltaña, and Balces anticlines (Fig. 1) and the detachment anticlines along the Sierras Exteriores thrust front further west (Millán et al., 2000). Their fold axes plunge to the north, where their terminations define a structural depression (Fig. 1).

The Serres Marginals Thrust Sheet is characterized by short-wavelength folds and thrusts involving an incomplete and thin Mesozoic-Paleogene succession unconformably covered by upper Eocene-Oligocene growth sediments. The synorogenic Upper Cretaceous carbonates progressively thin southwards from a few hundred meters in the northern imbricates to a few tens of meters in the most frontal ones (Fig. 1). These Upper Cretaceous sediments unconformably overlie the Jurassic carbonates and even the Triassic evaporites that were tilted northwards and partially or totally removed in the south by erosion (Martín-Chivelet, et al., 2019). In the Serres Marginals Thrust Sheet, the middle Eocene sediments are absent, except for in the most frontal imbricates, contrasting with the thick succession of middle Eocene carbonates to the west of the salient, in the Sierras Exteriores thrust front. These carbonates deposited coevally with the slope and basinal sediments of the Ainsa-Jaca basins (Fig. 1). The thin to absent middle Eocene interval was caused by structural relief and salt inflation of the Triassic salt in response to evacuation from the bottom of the Peña Montañesa Montsec Thrust Sheet. The thick salt, together with the thin Mesozoic succession, favored the development of detachment anticlines and diapirs (Poblet et al., 1998; Cofrade et al., 2023; Santolaria et al., 2017). The Serres Marginals and Peña Montañesa-Montsec thrust sheets are at present above an autochthonous succession of Paleocene and Eocene sediments in continuation with the Ebro foreland Basin, as shown by well and seismic data (Muñoz et al., 2018)(Fig. 1C).

North of the South-Central Pyrenean Thrust Salient, the basement rocks form an antiformal stack, classically referred to as the Axial Zone. This antiformal stack consists of three main basement-involved thrust sheets, which from top to bottom are the Nogueres, Orri and Rialp (Fig. 1; Muñoz, 1992). They were transported to the South together with the cover thrust sheets located toward the foreland. The Nogueres thrust sheet has the same structural position as the basement of the Gavarnie thrust sheet further west, but the Upper Triassic salt is absent in the Gavarnie thrust sheet, and the Upper Cretaceous limestones unconformably overlie the Paleozoic rocks, with the edge of the salt detachment highly oblique to the overall Pyrenean trend (Fig. 1). In map view, the transition from preserved Upper Triassic evaporites above the basement units in the east to areas where these evaporites are absent in

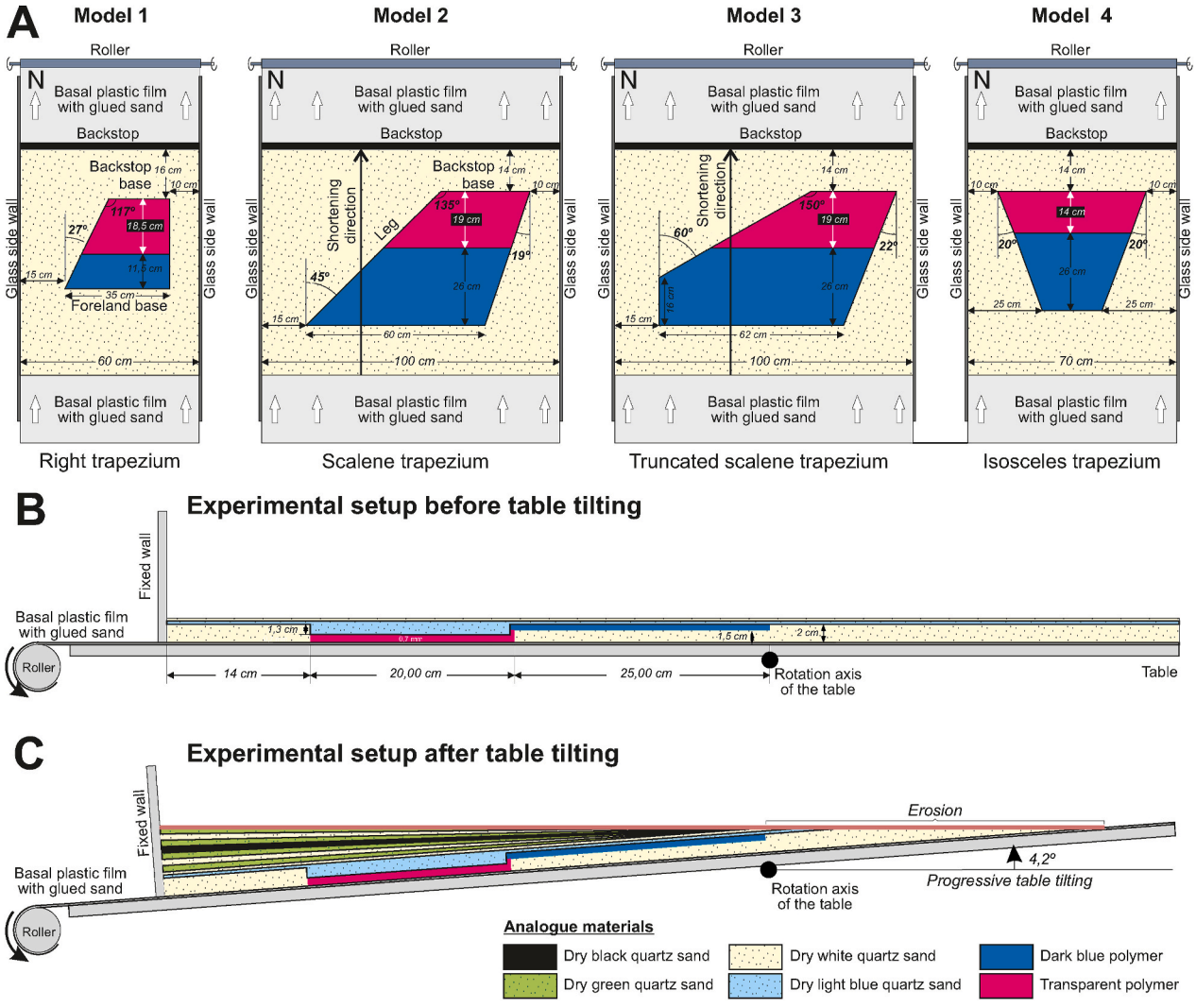

Fig. 2. A) Overhead sketches showing the setup of the selected models presented in this work. Note the different geometry of the trapezium shaped silicone polygons in each model. B) Representative cross-section of a model setup showing the configuration of the silicone layers before plate tilting. C) Schematic cross section showing the distribution and geometry of materials after base-plate tilting and before the onset of the contractional deformation that was transmitted from a non-stretchable plastic film attached to a metal roller fixed to a computer-controlled servomotor.

the west coincides with a significant structural bend of the structures from WNW-ESE to N–S (Fig. 1).

3. Experimental methodology

An experimental program, consisting of four primary models, was conducted at the Geomodels Analogue Modelling Laboratory at the University of Barcelona, to examine the influence of viscous detachment geometry on the development of oblique structures in salt-detached fold-and-thrust belts. Three additional models were performed to assess setup and boundary conditions but are not included here. This study was inspired by the structural evolution of the South-Central Pyrenean Thrust Salient, with a focus on the angle between the oblique edges of the viscous detachment and the shortening direction.

3.1. Experimental program design and procedure

The experiments employed the "subduction model" configuration developed by Graveleau et al. (2012). Instead of using a moving wall to drive the contractional deformation, a non-stretchable basal plastic film affixed to a computer-controlled servomotor, generated contractional deformation in the model (Fig. 2). As the basal film was rolled at a constant velocity of 4 mm/h, the fixed wall acted as a backstop at the base of which a velocity discontinuity localized the rooting of contractional structures (Fig. 2). The sandbox, with varying widths depending on the model, was confined by two fixed glass walls on the sides (Fig. 2A). We utilized the subduction model setup, also known as conveyor-type or pull-type, to mitigate issues related to the deformation of the rigid wall when pushing the sand pack, given the substantial width of the models. Furthermore, this approach aligns more closely with the boundary conditions of the natural prototype. In principle, de difference with push-type or indentation experiments is primarily a matter of reference frame (Buiter, 2012; Graveleau et al., 2012).

The parameter under scrutiny was the geometry of the salt basin. Various salt basins with trapezium geometries were tested to understand how the trends of their boundaries in relation to the shortening direction influenced the propagation of contractional deformation and the vertical axis rotation of resulting structures. The orientation and angle of the trapezium's lateral edges with respect to the shortening direction were determined based on geological constraints. This selection aimed to test the uncertainties associated with their accurate reconstruction before the onset of contractional deformation (Fig. 2A). Conversely, certain orientations were deliberately chosen to deviate from the reconstructed orientations, serving the purpose of examining differences between model results and observations.

The trapezium viscous detachment was segmented into two parts to replicate the control on salt distribution exerted by extensional faults of the Pyrenean rifted margin before the onset of the contractional deformation. Model construction began with an inner transparent silicone layer overlaying the basal plate with a specific trapezium geometry (Fig. 2A and B). This inner silicone layer, 7 mm thick, was surrounded by white quartz sand throughout the sandbox (Fig. 2A and B). The inner silicone was covered by an 8 mm thick blue sand layer while the rest of the model was covered by an 8 mm thick white sand layer (Fig. 2B). A second 5 mm thick blue silicone layer was added in front of the inner and lower one following the trapezium geometry of the salt basin (Fig. 2B). This outer silicone layer was surrounded by white sand except over the inner silicone, where the added sand was blue (Fig. 2B). Both silicone layers represent the same Triassic evaporite level offset by an Early Cretaceous extensional fault, and the blue sand above the inner silicone represents the synrift basin. Such a configuration reproduces the rifted margin before tectonic inversion and could correspond to the extensional faults along the Cotiella-Bóixols thrust front. After that, two additional 3 mm thick blue and white layers were added covering the entire model to simulate the lower postrift Upper Cretaceous succession in the Southern Pyrenees (Fig. 2B).

Then, the rig was systematically tilted 0.6° towards the backstop before the deposition of each layer of the following unit formed by alternating green, white, and black quartz sand, reaching 4.2° tilting after deposition of the entire unit (Fig. 2C). This wedge-shaped unit simulates the northward thickening of the Upper Cretaceous sediments in the southern Pyrenees, including most of the postrift succession and the first foreland basin deposits. This sand wedge was confined between the backstop and the rotation axis of the table that was located at 59 cm from the backstop, at the front of the silicone trapezium. The uplifted area beyond the rotation axis was subsequently scraped off at the regional elevation of the last sand layer of the wedge, eroding part of the underlaying pre-wedge units (Fig. 2C). This geometry simulates the erosion of the forebulge that occurred at Late Cretaceous times by lithospheric flexure during the early stages of contractional deformation (Fig. 2C). Finally, a 3 mm thick layer of reddish sand covered the entire model simulating the unconformable Paleocene succession in the Pyrenean foreland (Fig. 2C). This final configuration reproduces the stratigraphic template at early Eocene times before the development of the South-Central Pyrenean Thrust Salient as deduced from the construction of partially restored cross sections (Muñoz, 2002). Total shortening reached 22 cm, and syn-contractional sedimentation and erosion were not considered in any of the models.

Upon completion of the experiment, the models were covered by a thick post-kinematic unit to preserve topography and prevent silicone-related movement. Models were preserved and serially sliced after 24–48 h, with manual cross-section cuts at 1 cm intervals.

3.2. Analogue materials and scaling

The materials used in the experimental program were those classically used in analogue modelling: quartz sand to simulate the brittle behavior of upper crust rocks (Lohrmann et al., 2003); and a silicone putty (polydimethylsiloxane or PDMS) to simulate the viscous behavior of salt (Dell'Ertole and Schellart, 2013).

The 99.8% pure quartz sand has a mean grain size of 199 μm and a sub-rounded grain shape. It has a bulk density of 1500 kg/m^3, a mean coefficient of friction (φ) of 0.59, an average angle of internal friction ($^{\varphi}$) of 30–35°, and a low apparent cohesive strength of ~78–142 Pa (ring shear test, Ferrer et al., 2017).

White and colored sands have the same mechanical properties and were used to depict the location and style of the main structures.

The silicone made by Bluestar has an average density of 972 kg /m^3 and a viscosity of $1.6{\cdot}10^4$ Pa s at laboratory strain rates and room temperature (values provided by Dell'Ertole and Schellart, 2013). Transparent and blue silicones have identical mechanical properties.

The models were dynamically scaled in accordance with the methodology proposed by Hubbert (1937), Davy and Cobbold (1988), and Schellart (2000). The scaling parameters are shown in Table 1.

In all models, sand was glued to the non-stretchable plastic film at the base to increase basal friction (Pla et al., 2019), with the friction value at the base equal to the internal sand friction in the frictional domain (Larroque et al., 1995).

3.3. Recording techniques

Overhead and oblique time-lapse pictures, captured every 60 s with a high-resolution digital camera, documented the kinematic evolution of the models during deformation. Models' surface topography was recorded every 2 cm of shortening using a submillimeter resolution white light scanner (*SidioPro* from *Nub3D*). Animations of the models based on these surfaces can be found in the supplementary material. The vertical sections cut at 1 cm intervals at the experiments' end were photographed using high-resolution digital cameras to reconstruct and analyze the final structure of the models and their along-strike structural variation.

Table 1
Dynamic scaling of the analog modeling experimental program. The scaling ratio is the Model to Nature ratio of a given magnitude or parameter. σ, deviatoric stress (Pa); ρ, density (kg/m3); g, gravitational acceleration (m/s2); L, length (m); ε, strain rate (s-1); η, viscosity (Pa·s); t, time (s); V, velocity (m/s). *Mean apparent cohesive strength.

Parameter	Equation	Model	Nature	Scaling ratio
Length		1 cm	1 km	10^{-5}
Density				
Sand/Brittle Rocks		1500 kg/m^3	2567 kg/m^3	0.58
Polymer/Décollements		972 kg/m^3	2200 kg/m^3	0.4
Gravity		9.8 m/s^2	9,8 m/s^2	1
Cohesion		110 Pa*	50×10^6 Pa	2.2×10^{-6}
Deviatoric stress	$\sigma = \rho \cdot g \cdot L$	121 Pa	2.34×10^7 Pa	5.2×10^{-6}
Viscous layer viscosity		1.6×10^4 Pa s	10^{18} Pa s	1.6×10^{-14}
Strain rate	$\varepsilon = \sigma/\eta$			3.24×10^8
Time	$t = 1/\varepsilon$	1 h	37000 y	3.1×10^{-9}
Velocity	$V = L \cdot \varepsilon$	0.5 cm/h	13.5 mm/y	3.24×10^3

4. Experimental results

The following section describes the experimental results, primarily focusing on the selected overhead views of the models at various evolutionary stages and the final cross sections. The main features of the models will be described, but our primary emphasis will be on the structures developed in the transitional areas between the frictional and viscous domains. To aid in the description and subsequent comparison with the natural prototype, we established a coordinate system where the backstop corresponds to the north (Fig. 2A).

4.1. Model 1

In Model 1, the viscous domain is characterized by a right trapezium, widening toward the foreland with an eastern leg (or lateral edge) parallel to the shortening direction. The western leg forms an angle of 27° with this direction and an internal angle of 117° with the edge of the trapezium adjacent to the backstop (Fig. 2A). In the early stages of shortening, a thrust (T1 in Fig. 3A) formed with a continuous E-W trend hindward of the northern edge of the inner silicone polygon (Fig. 3A). Deformation progressed forward, and after 60 mm of shortening, once it reached the silicone, the entire sand wedge above the viscous detachment was internally deformed by layer-parallel shortening, as commonly observed (Koyi et al., 2004; Santolaria et al., 2021). The thrust front then jumped to the pinch-out of the outer silicone polygon (foreland edge of the trapezium) synchronously with nucleation of a structure over the step between the two silicone layers (Fig. 2A and 3B, S1). Regardless of their trend – parallel or oblique to the shortening direction - the lateral edges of the viscous domain were activated as strike-slip faults (Fig. 3B), with the eastern one as a left-lateral strike-slip fault system and the western one as a single right-lateral strike-slip fault. Immediately afterward (Fig. 3B), thrust 2 developed in the western frictional area (T2w) and propagated into the viscous domain (T2c). In the eastern frictional domain, a second thrust (T2e) formed with a convex geometry. It struck with an E-W trend in the frictional domain and turned to a NE-SW trend in the transitional area with the viscous domain (Fig. 3B).

At 78 mm of shortening, thrust 3 developed in the western frictional area (T3w) to continuously build up the brittle thrust wedge (Fig. 4a). This thrust showed an WNW-ESE trend, oblique to the previous ones, and formed a sharp bend to a N–S trend in the transitional area with the viscous domain (Fig. 3C). This bend resulted from the linkage of the eastern tip of T3w with the active thrust front at the southern edge of the silicone polygon, also referred to the frontal décollement pinch-out (Costa and Vendeville, 2002). Where these two thrusts connected, a new thrust propagated into the sand wedge above the viscous detachment, located over the step between the two silicone layers (T3c in Fig. 3D). This structure had already initiated earlier, as revealed by the rising topography (Fig. 3C–S1). At that moment, the western strike-slip fault became inactive and experienced a southward translation and a clockwise vertical-axis rotation (hereinafter VAR). In fact, this fault was a tear fault bounding the viscous detachment at the early stages, with an oblique slip because of the southward displacement and synchronous uplift of the sand pack above the viscous detachment (Fig. 3C and 4b). Strain compatibility between forward displacement of the sand wedge above the viscous domain and the divergent lateral edges of the silicone trapezium resulted in a divergent displacement pattern in the viscous domain. This displacement is emphasized in the models by the orientation of the scratch lines done by the scraper during levelling of the sand layers (Fig. 3C and D). These lines were initially parallel to the lateral edges of the sandbox and, thus, to the shortening direction.

In the hanging wall of the T3w thrust, an anticline developed, bounded northwards by two NW-SE to N–S trending backthrusts, at an angle with the edge of the silicone polygon but not rooted in the silicone (Fig. 3C–F and 4b). Along the eastern edge of the silicone polygon, the strike-slip fault progressed southwards to connect with the frontal structure. It connected with the T2e thrust by a push-up structure oblique to the edge of the silicone. Synchronous thrusting in the western brittle wedge (T3w and T2w) occurred together with the internal deformation of the sand wedge above the viscous detachment. The SW corner of the silicone polygon deformed into a N–S trending anticline in continuation with the thrust front. It plunged northward, defining a depression between it and the southern tip of thrust T3w (Fig. 3D–F, S1). This SW structure acquired a prominent arcuate geometry as shortening progressed because of the divergent displacement pattern in the viscous domain and the related vertical-axis rotations (Fig. 3C–D). This rotation triggered the formation of NE-SW trending extensional faults (Fig. 3D and E).

With continued shortening, the central thrust front advanced relative to the footwall but retreated with respect to the backstop because of the internal deformation. An out-of-sequence thrust (T3c) nucleated behind the frontal thrust and accommodated a significant amount of shortening within the thrust wedge above the viscous domain (Fig. 3D). After 158 mm of shortening, thrust T3c continued to be active (Fig. 3D and E). This thrust developed synchronously with the main activity of the SW thrust salient and the clockwise VAR near the western boundary of the viscous domain. T3c died out eastward and was relayed by an anticline in the hanging wall of the thrust front. At the eastern edge of the viscous domain, the N–S trending left-lateral strike-slip fault continued to be active. However, a lateral ramp of the frontal thrust developed parallel to the strike-slip fault, taking the shortening component related to the divergent displacement pattern of the viscous domain (Fig. 3D and E).

At 165 mm of shortening, a new thrust (T4w) formed in the western frictional area, with a similar geometry to thrust T3w but with a shorter N–S trending portion in the transitional area to the viscous domain, as constrained by the available space (Fig. 3E). This lateral structure connected with the N–S trending portion of the western thrust front of the viscous domain, defining a continuous thrust salient with a structural depression that coincided with the edge of the silicone (Fig. 3E and F). In the eastern lateral structure, a diapir pierced the surface. At 193 mm of shortening, a new thrust developed in the eastern frictional domain that intersected the N–S trending structure at the diapir (T4e, Fig. 3F). The thrust front in the viscous domain advanced slightly, mainly in its eastern part.

The cross-sectional structural style of Model 1 in the frictional domains was characterized by a brittle Coulomb wedge with a taper angle of about 25° formed by the stacking of thrust sheets that generally developed in a foreland-propagating sequence, although synchronous thrusting occurred (Fig. 4a and e). The notably high wedge taper angle observed here is indicative of wedges developed under high basal friction conditions, such as those observed in models with glued sand on the

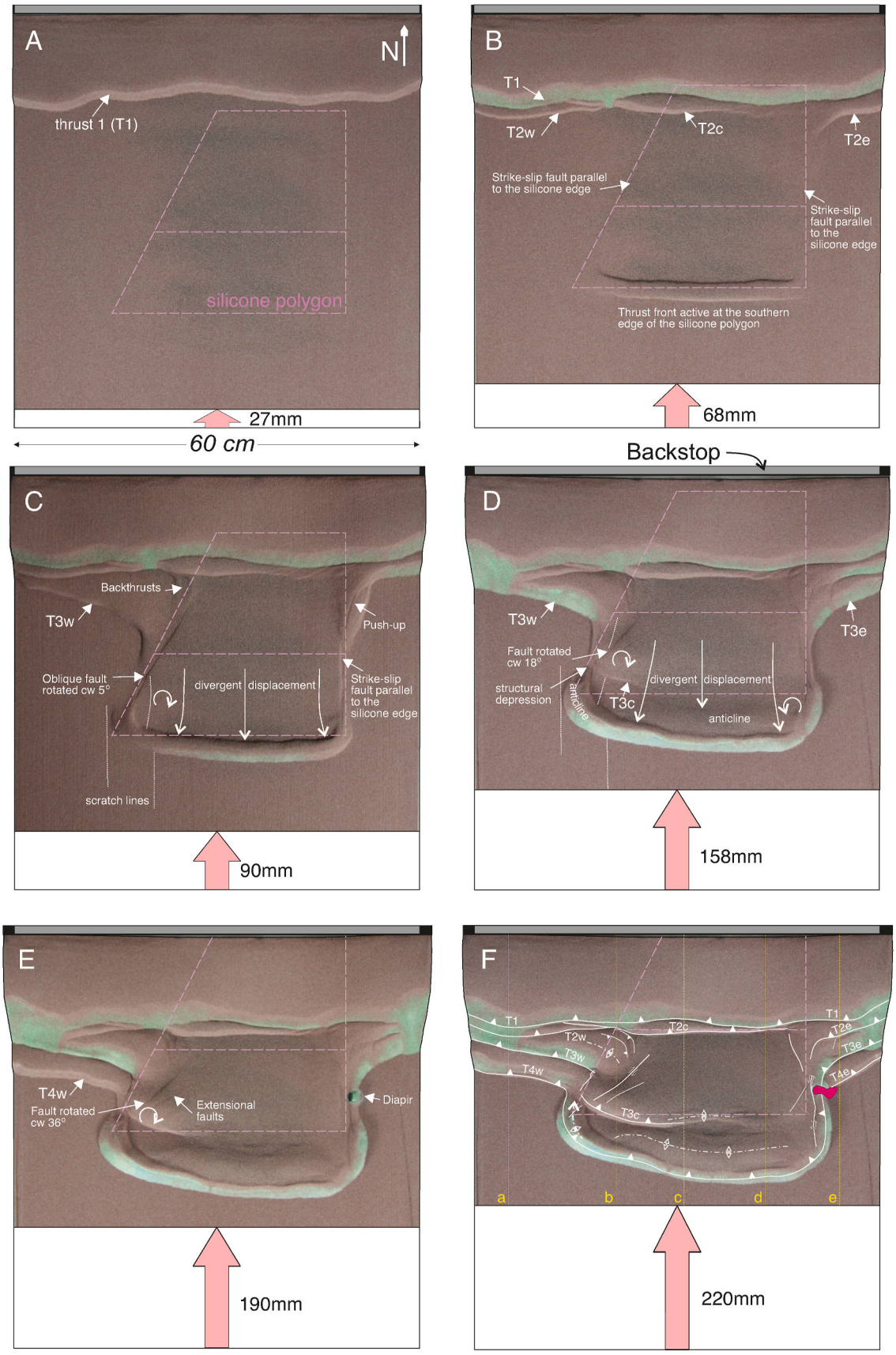

Fig. 3. Selected top view images of Model 1 with incremental shortening and interpretation of the model (F). The location of the undeformed position of the silicone polygon as well as the internal step between the two silicone layers are indicated by pink dashed lines, and the labelled faults are explained in the text. Green colour corresponds to the slumped lower green layers. Illumination from the SE. Yellow lines in Fig. 3F correspond to the location of the final cross sections in Fig. 4. (For interpretation of the references to colour in this figure legend, the reader is referred to the Web version of this article.)

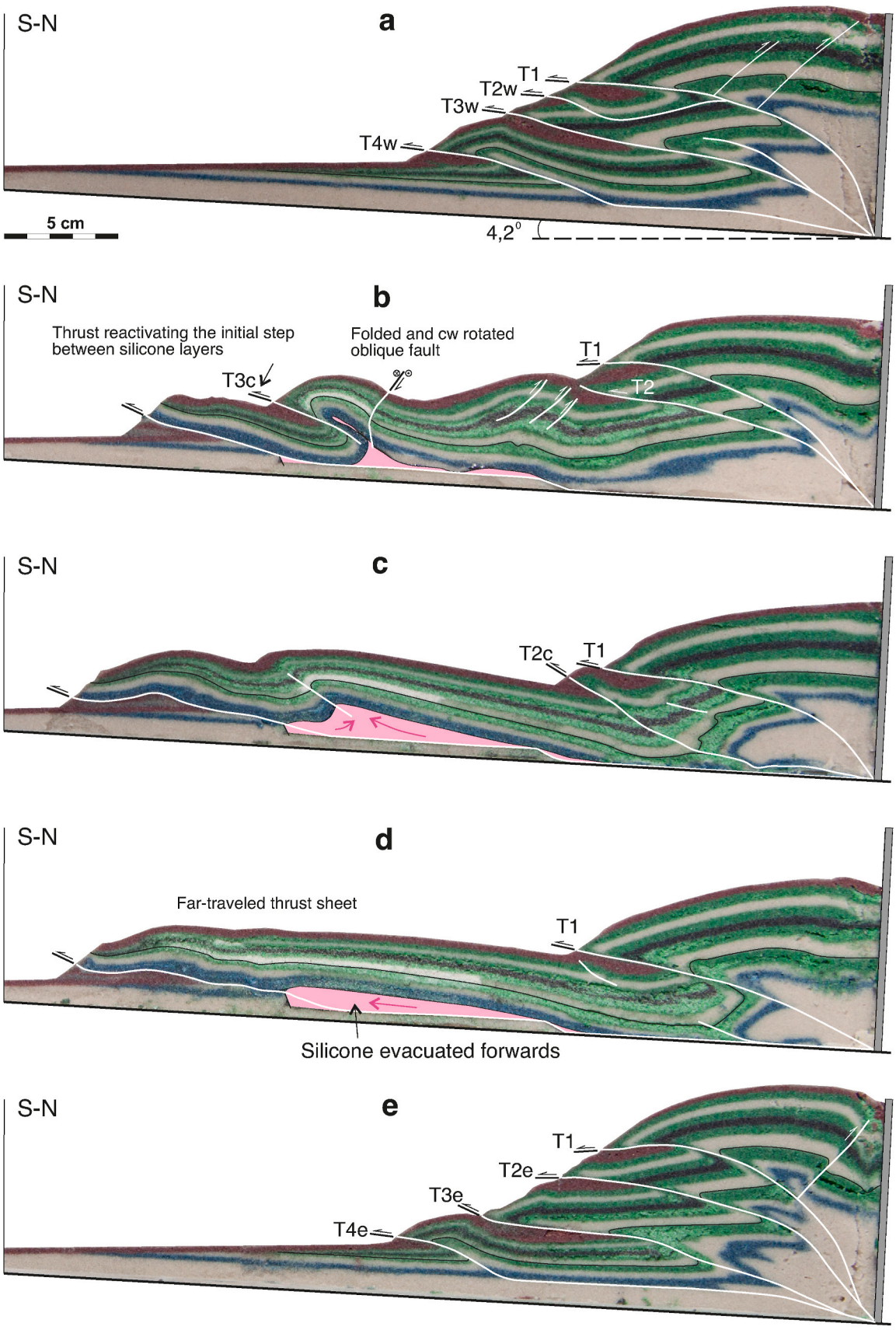

Fig. 4. Representative cross sections across Model 1 illustrating the along-strike variation of the structural style between frictional and viscous domains. Both the transparent and blue silicone layers are combined and highlighted in pink, and the labelled faults are explained in the text. The location of the cross sections are labelled on Fig. 3F. (For interpretation of the references to colour in this figure legend, the reader is referred to the Web version of this article.)

mylar film at the base (Huiqi et al., 1992). In contrast, the thrust wedge above the viscous detachment showed a lower taper, involved fewer thrusts and displayed a lower topography in the hinterland (Fig. 4b-d, movie S1).

4.2. Model 2

In Model 2 the viscous domain is characterized by a scalene trapezium with the legs forming angles of 45° (west) and 19° (east) with the shortening direction. The western leg has an internal angle of 135° with the backstop edge of the trapezium. (Figs. 2 and 5). The initial thrust in the frictional domain, labelled thrust 1, formed after 16.5 mm of shortening but, contrary to model 1, T1 did not extend into the viscous domain. Instead, deformation was transmitted forward into the sand wedge above the silicone domain, leading to the development of an anticline just south of the step connecting the two silicone layers (Figs. 2 and 5A-B, S2). This observed pattern is linked to the lower distance between the backstop and the northern edge of the silicone trapezium.

At 30 mm of shortening, the thrust front rapidly progressed to the southern pinch-out of the silicone, occurring earlier than in the previous model, because the shorter distance between the northern silicone edge and the backstop. However, this shift was limited to the eastern portion.

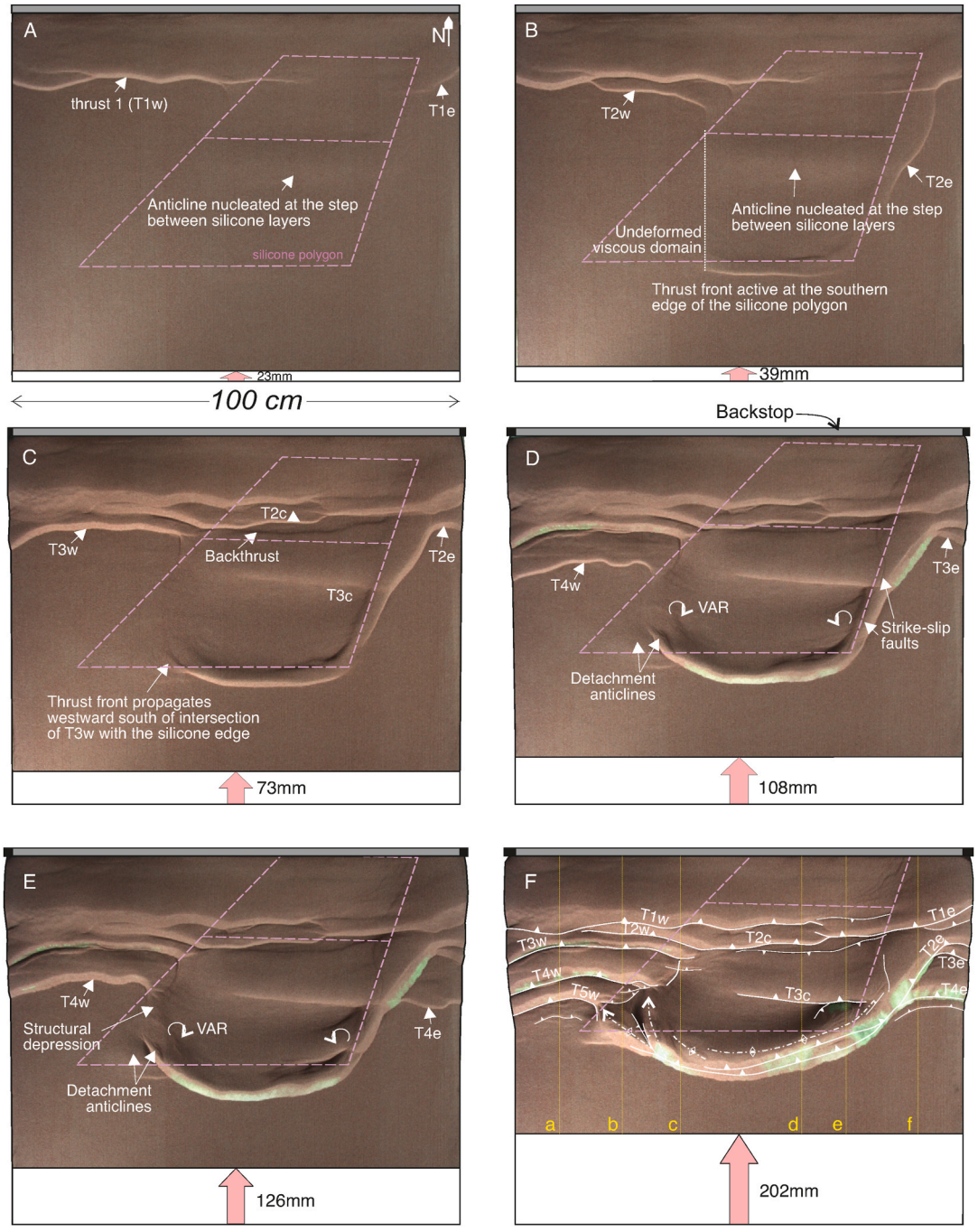

Fig. 5. Overhead evolution and interpretation of Model 2. The pink polygons indicate the shape and original location of the silicone polygon and the internal step between the two silicone layers, and the labelled faults are explained in the text. Green colour corresponds to the slumped lower green layers. Illumination from the SE. Yellow lines in Fig. 5F correspond to the location of the final cross sections in Fig. 6. (For interpretation of the references to colour in this figure legend, the reader is referred to the Web version of this article.)

The southwestern corner of the viscous domain remained unaffected, and the western boundary of the deformed viscous domain ran parallel to the shortening direction along a diffuse boundary. This boundary was defined by a line connecting the western tip of the thrust front of the viscous domain with the intersection of the active thrust front within the western frictional domain and the lateral edge of the silicone polygon (Fig. 5B, movie S2). As shortening increased, a new thrust developed in the western frictional area (T2w in Fig. 5B), also showing a sharp bend to a short N–S trend portion as it connected with the edge of the silicone polygon. Synchronously, the thrust front along the southern silicone edge propagated westward to the southward prolongation of the intersection between thrust T2w and the silicone edge (Fig. 5B). The eastern edge of the silicone polygon evolved to a transpressional zone, where a highly oblique thrust subparallel to the silicone edge formed, connecting with the thrust front in the eastern frictional domain (T2e in Fig. 5B).

As the model progressed, at 52 mm of shortening, a new thrust (T3w) formed in the western frictional domain and showed similar geometric features as described for older thrusts. This led to the gradual reduction of the triangular undeformed area at the SW corner of the silicone polygon, as new thrusts continued to develop in the western frictional wedge and the thrust front of the viscous detachment propagated westward (Fig. 5C and D). Concurrently, the thrust wedge above the viscous detachment underwent internal deformation with the structural growth of the central anticline (and related thrust and backthrust), the propagation of thrust T2c into the central domain, and the imbrication of the eastern thrust front (T2e and T3e) (Fig. 5C–D and 6). After 100 mm of shortening, new silicone-cored detachment anticlines formed along the thrust front, laterally linked with each thrust in the western frictional domain (Fig. 5D–E). These anticlines formed initially with a NW-SE trend and a NW plunge, but acquired a more N–S trend due to clockwise VAR resulting from the divergent displacement at the foreland corners of the silicone polygon (Fig. 5D–E). The areas of linkage between the thrusts of the western frictional wedge and the frontal detachment anticlines corresponded to structural depressions, aligned parallel to the oblique silicone edge (Fig. 5E–F). Simultaneously, near the eastern boundary of the thrust salient, a system of minor strike slip faults developed, connecting the eastern imbricate wedge with the frontal structure along and parallel to the edge of the silicone (Fig. 5D). The westward plunge of the anticline in the middle of the silicone polygon became more prominent.

After 125 mm of shortening, the frontal part of the thrust wedge above the viscous domain was internally deformed as shown by the decrease in distance between the thrust front and thrust T3c (compare Fig. 5D, E and F). This internal deformation increased eastward, resulting in the WSW-ENE trend of the eastern part of the thrust salient, where two synchronous thrusts developed. While the wedge above the viscous detachment deformed and reduced in width, the adjacent thrust wedges in the frictional domains accreted new thrusts and advanced forwards. Consequently, the salient geometry of the most frontal structure became less prominent than in previous stages (see S2).

The final stage illustrated that structures formed in transitional areas between the frictional and viscous domains displayed an oblique trend with respect the silicone edges. In the western transitional zone between the frictional and viscous domains, structures formed with a NW-SE to N–S orientation at a significant angle to the edge of the silicone. These structures evolved and connected as shortening continued. The structural depression that formed between the structures of both domains also developed a slightly oblique orientation relative to the initial orientation of the lateral edge of the silicone polygon, resulting from the deformation-induced slight change in orientation (Fig. 5F). Similarly, the thrust and related structures that initially developed along the eastern edge were also transported progressively forwards and their final trend also deviated from the initial orientation of the silicone edge. The final geometry of the thrust front along the southern edge of the viscous detachment changed significantly along strike, evolving from an imbricate stack in the east, to a single large displacement thrust, to a system of laterally stacked detachment anticlines in the west (Fig. 6). In this model, the base of the upper silicone layer had a small depression resembling a minor extensional fault near its southern edge. This feature was unintentionally created during the model-building process. However, it had no impact on the evolution of the frontal structures, as the silicone accumulation was preserved as a dead zone in the footwall of the sole thrust (Fig. 6).

The silicone exhibited an overall tendency to flow forward, facilitating the development of a simple, far-travelled thrust sheet (Fig. 6c). Nonetheless, the inflated salt area in the frontal areas of the viscous domain, coupled with the thin overburden, also facilitated the formation of thrust imbricates and tight detachment anticlines. This, in turn, contributed to the structural relief observed during the internal deformation of the thrust wedge by break-back thrust sequences (Fig. 6).

4.3. Model 3

In Model 3, the geometry of the silicone polygon was a truncated scalene trapezium with a larger internal angle of 150^{o} between the western leg and the backstop edge, resulting in a more extensive viscous detachment surface compared to all other models (Fig. 2A). The model results were akin to those observed in Model 2 (See S2 and S3).

After 35 mm of shortening, a first E-W trending thrust developed uniformly along the model without apparent segmentation across the lateral edges of the silicone polygon (T1 in Fig. 7A). Nevertheless, the amount of shortening accommodated along T1 diminished eastward above the viscous detachment because a portion of the shortening was transferred forward, localized above the central step between the two silicone layers and at the southern silicone pinch-out (Fig. 7A). A central thrust (T3c) originated at the step between the two silicone layers and connected with a newly formed thrust in the eastern frictional wedge (T3e) along an oblique SW-NE segment within the transitional zone with the viscous domain. T3e emerged at a greater distance into the foreland than expected based on the positions of the preceding thrusts, suggesting that the location of T3e may have been influenced by the presence and positioning of T3c (Fig. 7A–B).

As shortening continued, new forward-propagating thrusts formed in the western frictional wedge (T2w and T3w). In the transitional area of the western frictional domain, each thrust curved to a N–S trend and, further south, connected to the N–S trending folds developed above the viscous detachment (Fig. 7C). These folds displayed a northward plunge and together with their related thrusts they emerged from the thrust front (Fig. 7C). Thrusts of the frictional domain and detachment folds of the viscous domain connected at the silicone edge and formed a structural depression. The thrust front at the southern silicone pinch-out migrated westward as new NW-SE to N–S trending structures formed, connecting with progressively younger thrusts in the western frictional wedge (Fig. 7C). Clockwise VAR occurred, larger than the anti-clockwise rotation observed at the eastern edge of the silicone polygon.

In the later stages of shortening (after 180 mm), the thrust wedge above the viscous detachment underwent internal deformation. Out-of-sequence thrusts formed north of the thrust front (T4c, backthrusts and related pop-up; Fig. 8c and d). Thrusts of the western frictional thrust wedge were also reactivated and propagated eastward into the viscous detached thrust wedge along the structural depression (Fig. 7D).

The evolution of structures in the transitional area of the eastern lateral edge of the silicone polygon was simpler than in the western counterpart. The silicone edge was activated as an oblique thrust since the early stages of shortening, and the thrusts in the eastern frictional thrust wedge merged into the oblique frontal thrust. The trend of this oblique frontal thrust progressively changed to form a higher angle with the shortening direction. The transitional area between domains featured a large anticline as successive frontal thrusts sheared in a break back sequence the overturned forelimb (Fig. 8e).

Serial cross-sections illustrate the along-strike structural differences controlled by the geometry of the viscous detachment (Fig. 8).

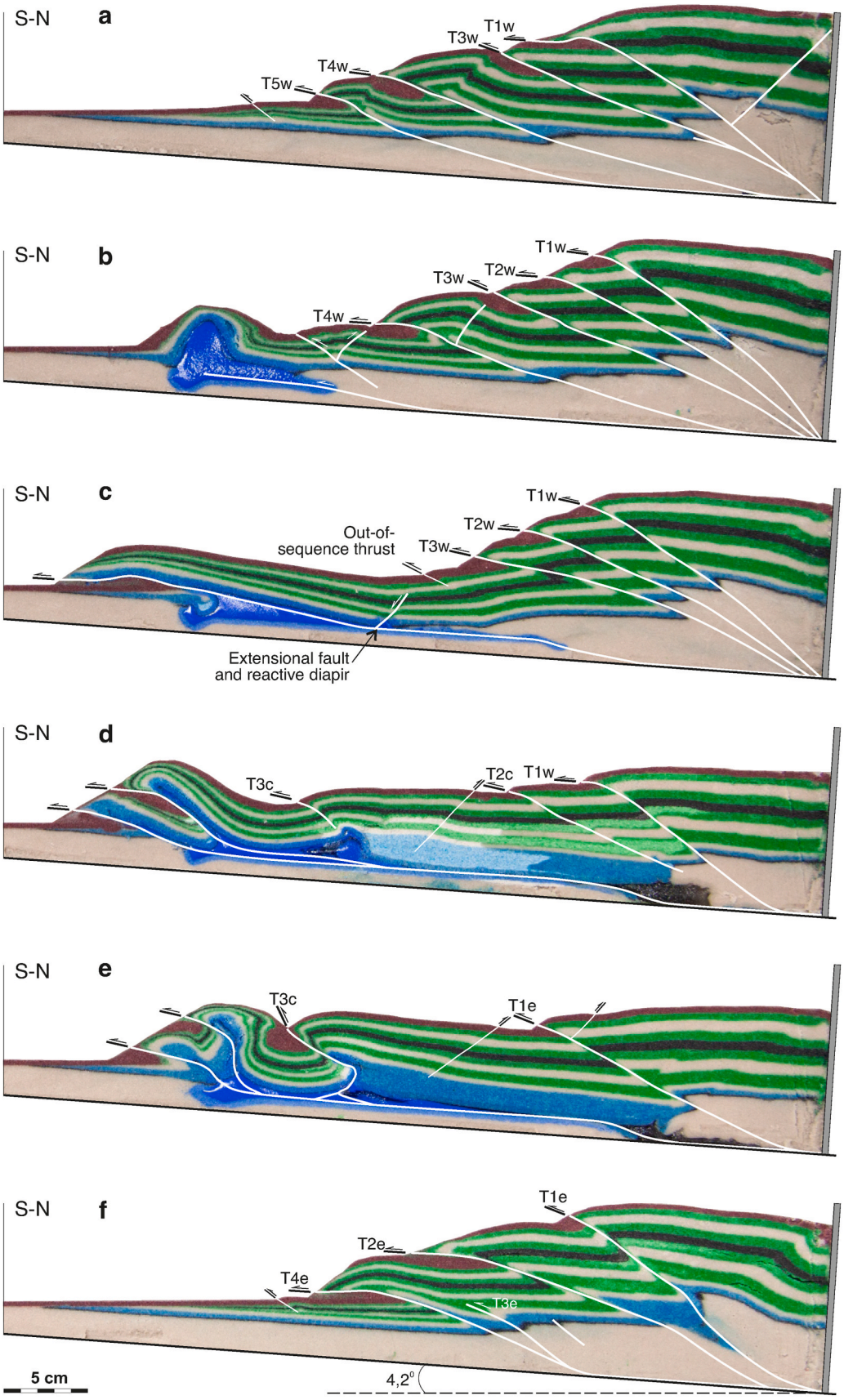

Fig. 6. Final cross sections across Model 2 illustrating the along-strike variation of the structural style between frictional and viscous domains. The black and bright blue are the lower and upper silicone layers, respectively, and the labelled faults are explained in the text. See locations in Fig. 5F. (For interpretation of the references to colour in this figure legend, the reader is referred to the Web version of this article.)

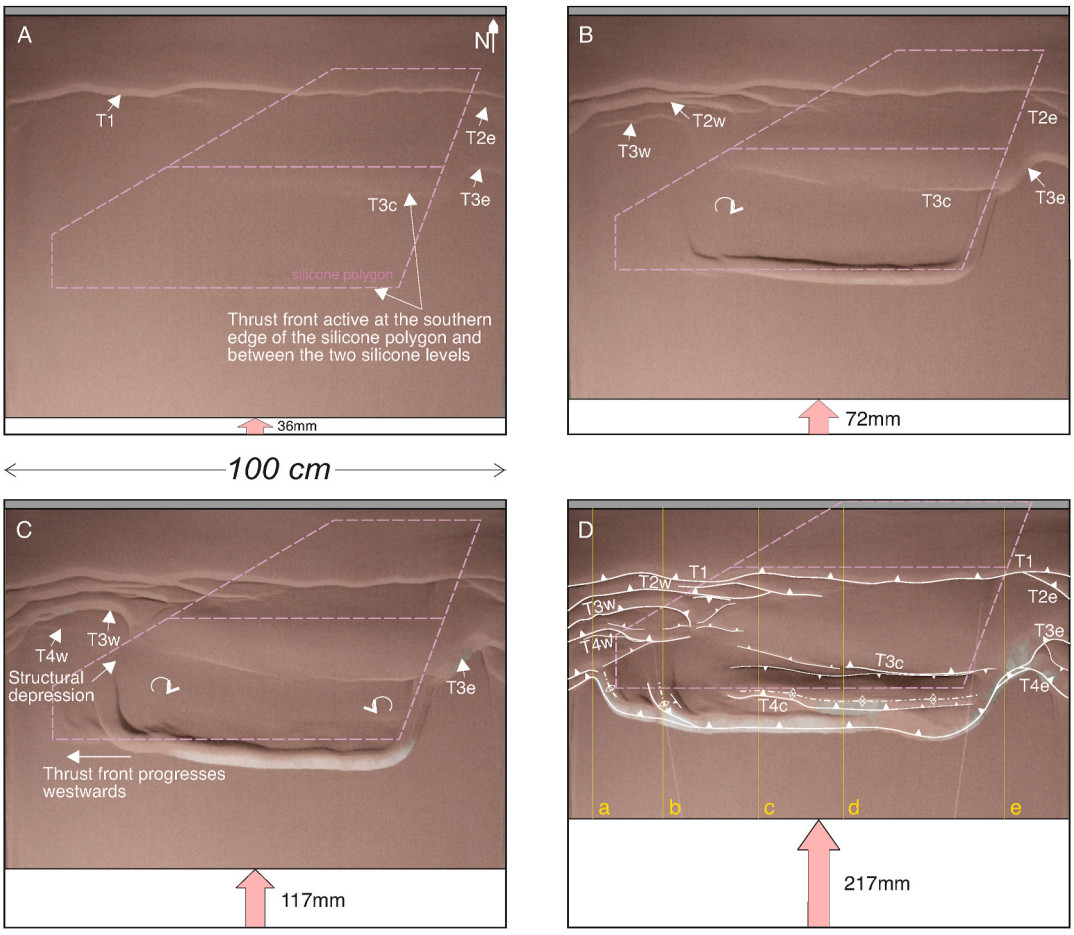

Fig. 7. Overhead evolution and interpretation of Model 3. The pink polygons indicate the shape and original location of the silicone polygon and the internal step between the two silicone layers, and the labelled faults are explained in the text. Green colour corresponds to the slumped lower green layers. Illumination from the SE. Yellow lines in Fig. 7D correspond to the location of the final cross sections in Fig. 8. (For interpretation of the references to colour in this figure legend, the reader is referred to the Web version of this article.)

4.4. Model 4

Model 4 is characterized by an isosceles trapezium with both lateral edges converging forward (Figs. 2 and 9). This symmetrical setup resulted in a symmetrical structural pattern during the contractional deformation.

After 25 mm of shortening, the first thrust (T1) developed along the entire model and the entire length of the silicone polygon was activated. Thrust T1 was segmented across the lateral edges of the silicone polygon, particularly on the eastern side (T1e). Simultaneously, the central step between the two silicone layers influenced the location of the second thrust in the adjacent frictional domains, occurring further into the foreland than might be expected, akin to Model 3 (T2w and T2e, Fig. 9A). These thrusts formed bends from E-W to NW-SE and NE-SW in the western and eastern transition zones, respectively, connecting with the silicone lateral edges at the southern prolongation of the northern corners of the silicone polygon. This emphasized the impact of the weak detachment geometry on the transitional areas between frictional and viscous domains (Fig. 9A). During these early stages of shortening, strike-slip faults formed along the northern portions of the lateral edges of the silicone polygon. However, they evolved quickly to oblique faults and backthrusts (Fig. 9).

At 50 mm of shortening, all the thrusts were active (synchronous thrusting). Afterward, the thrust wedge above the viscous detachment was deformed by out-of-sequence thrusts and anticlines that developed between the thrust front and thrust T2c (Fig. 9B–D). Tight silicone-cored detachment anticlines formed, and the silicone locally extruded to the surface (Fig. 9D).

In the transitional domain at both lateral sides of the viscous detachment, oblique antiformal stacks formed (Fig. 10b, e). They developed by the stacking of the oblique portion of the thrusts connecting the successive new thrusts of the frictional domains with the silicone edge, south of the northern corners of the silicone polygon (Fig. 9).

The final structure above the viscous domain comprised a far-travelled thrust sheet, featuring few thrusts and defining a horizontal surface taper (Fig. 10c, d). Most of the shortening occurred in the frontal structures, where out-of-sequence thrusts developed. A noteworthy observation from these model results is that the frontal thrust, which originated during the initial stages at the southern pinch-out of the silicone, became fossilized by the sand sourced from the hanging wall of the out-of-sequence thrusts (Fig. 10c, d). The frontal imbricates were entirely overridden by these thrusts, rendering them invisible in the top images (compare Figs. 9 and 10).

5. Discussion

The comparison of our model results to previous modelling studies and natural examples provides new insights into the influence of the inherited geometry of viscous detachments on salt-involved fold-and-thrust belts and the formation of thrust salients.

This experimental program was motivated by the structural evolution observed in the South-Central Pyrenees. The experimental setups were designed based on the main stratigraphic and structural features

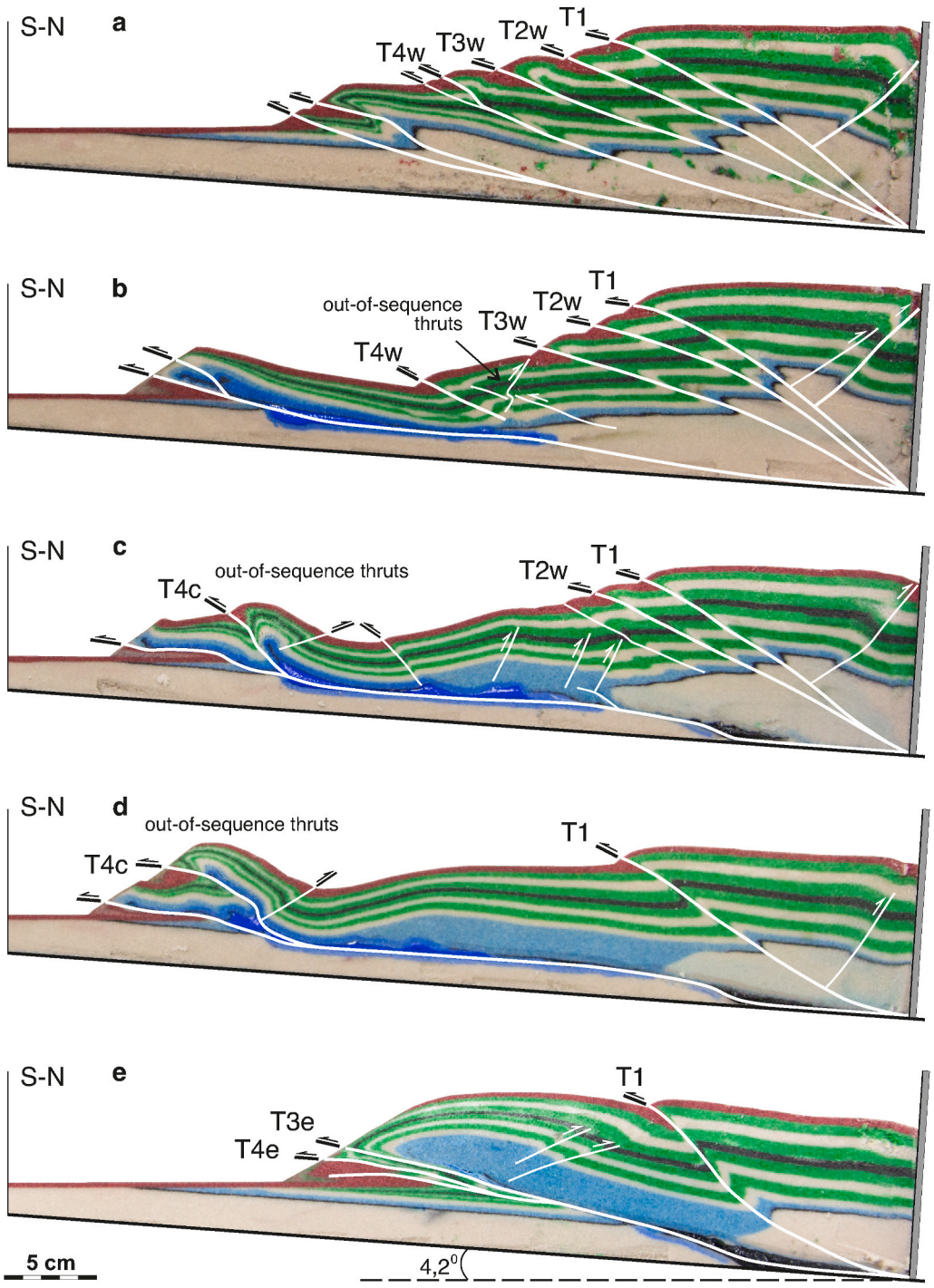

Fig. 8. Final cross sections across Model 3 illustrating the along-strike variation of the structural style between frictional and viscous domains. The black and dark blue are the lower and upper silicone layers, respectively, and the labelled faults are explained in the text. See locations in Fig. 7D. (For interpretation of the references to colour in this figure legend, the reader is referred to the Web version of this article.)

observed in the Pyrenean fold-and-thrust belt. Our model results successfully reproduced the main features of previous analogue modelling studies (see reviews by Graveleau et al., 2012 and Santolaria et al., 2024), as well as observations from other salt detached fold-and-thrust belts. Notably, our models introduced innovative ideas and conclusions arising from specific modelling configurations. The main difference of this work with previous analogue modelling studies is the combination of an initial wedge geometry of the sand package thickening towards the backstop above the silicone layer (Smit et al., 2003) with different geometries of the viscous detachment as modelled by many authors (i.e., Cotton and Koyi, 2000; Bahroudi and Koyi, 2003; Luján et al., 2003; Vidal-Royo et al., 2009; Wu et al., 2014; Li and Mitra, 2017; Borderie et al., 2018; Pla et al., 2019; Miró et al., 2023; Werf et al., 2023; Santolaria et al., 2024, among others).

5.1. Geometry of the structures and thrust sequence

The structural style of the models was largely dependent on the geometry and distribution of the viscous detachment. The initial sand wedge geometry used in our experiments facilitated the forward

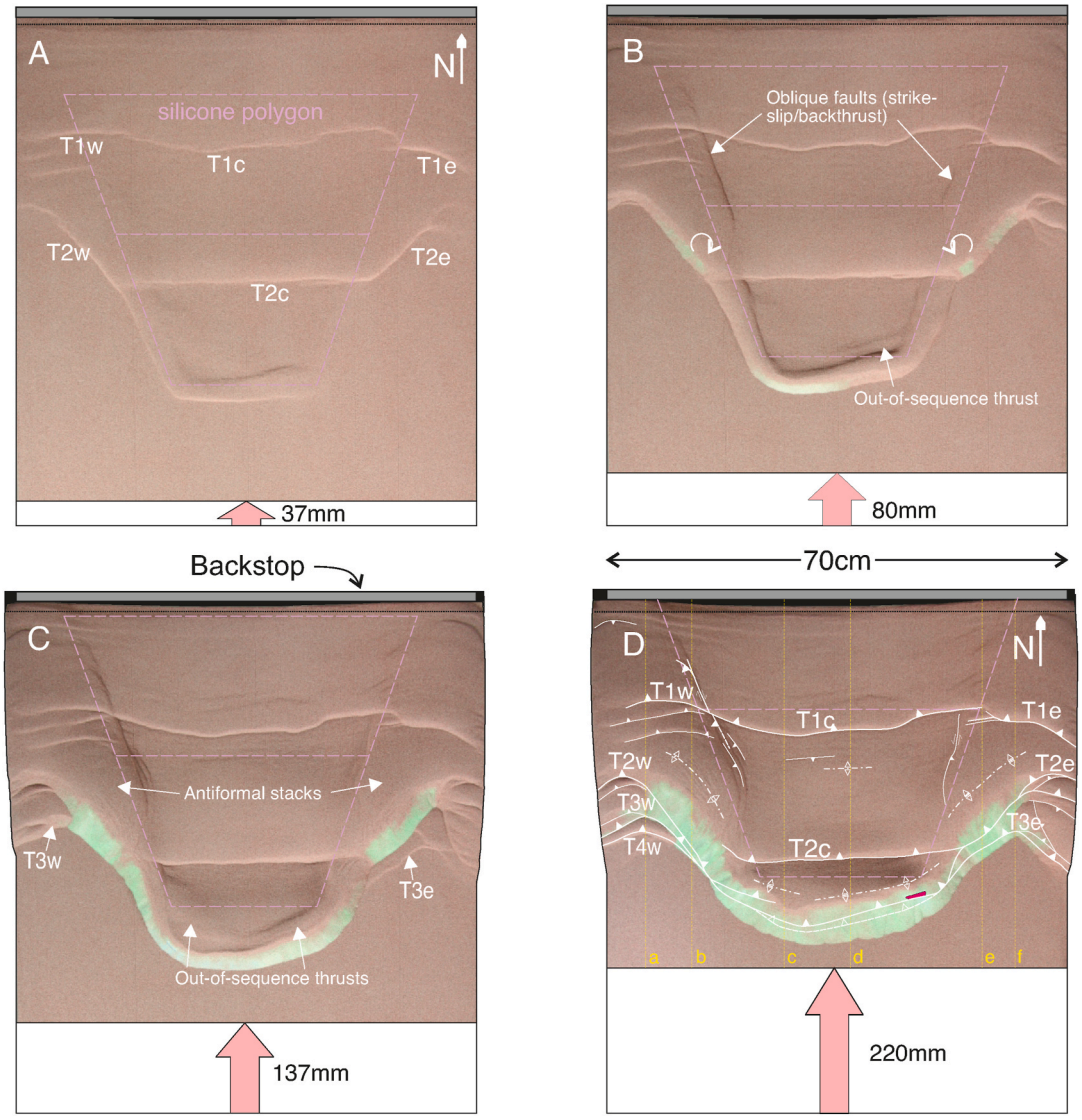

Fig. 9. Overhead evolution and interpretation of Model 4. The pink polygons indicate the shape and original location of the silicone polygon and the internal step between the two silicone layers, and the labelled faults are explained in the text. Green colour corresponds to the slumped lower green layers. Illumination from the SE. Yellow lines in Fig. 9D correspond to the location of the final cross sections in Fig. 10. (For interpretation of the references to colour in this figure legend, the reader is referred to the Web version of this article.)

propagation of deformation above the viscous detachment, causing the thrust front to advance early to the southern pinch-out of the silicone.

In all the models presented, the hinterland pinch-out of the silicone polygon was located in front of the backstop. Model 1 featured a silicone trapezium with its edge 2 cm farther from the backstop than in the other models (Fig. 2A). This spatial difference influenced the location and characteristics of the first thrust formed during the early stages of shortening. Whereas the first frontal thrust in Model 1 displayed a consistent strike and displacement, the initial thrust in other experiments was segmented across the lateral edges of the silicone polygon, and the displacement above the viscous detachment decreased due to the forward progression of deformation (Figs. 3, 5, 7 and 9). Moreover, this thrust emerged at a greater distance from the backstop in both frictional and viscous domains (Fig. 11). These observations indicate that the presence of a viscous layer influences deformation in the adjacent frictional domains, aligning with similar findings in the experiments by Li and Mitra (2017) and Borderie et al. (2018). At early stages of shortening both the area above the step between the two silicone layers and the forward pinch-out of the silicone polygon were activated (Fig. 6A, 7A and 9A and 11). Therefore, a prominent thrust salient formed since the early stages of contraction, also as observed in previous modelling studies (Cotton and Koyi, 2000; Luján et al., 2003; Li and Mitra, 2017; Werf et al., 2023; among many others).

As deformation continued, active structures above frictional and viscous detachments interacted with each other and tended to connect and link in the transitional areas. The nature of this interaction depended largely on the angle of the silicone edges relative to the shortening direction.

Strike-slip and tear faults developed along the lateral edges of the silicone polygon only when the angle of these edges with respect to the shortening direction was small ($<20^{o}$) (Figs. 3 and 9). These faults mainly developed at early stages and only persisted if the lateral silicone edge was parallel to the displacement vector (Fig. 3). Strike-slip faults formed along slightly oblique edges evolved into tear faults with an oblique reverse displacement (Fig. 9) or became inactive and passively deformed (Fig. 3).

At about 50 mm of shortening, the majority of thrusts became active, resulting in synchronous thrusting in all thrust wedges (Fig. 12). Thrusts within the frictional thrust wedges were activated concurrently with the development of the thrust front. In the thrust wedge of the viscous

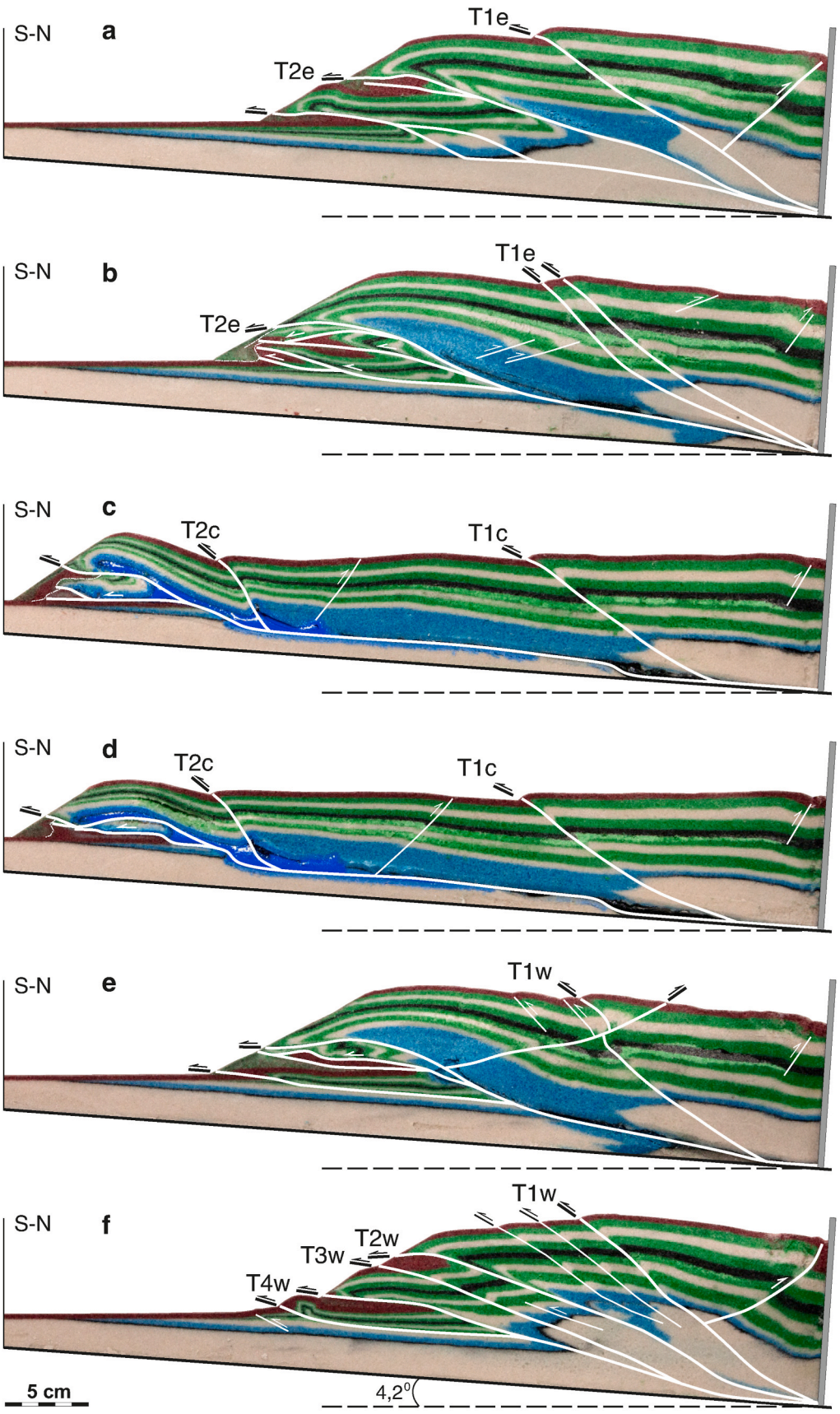

Fig. 10. Final cross sections across Model 4 illustrating the along-strike variation of the structural style between frictional and viscous domains. The black and dark blue are the lower and upper silicone layers, respectively, and the labelled faults are explained in the text. See location in Fig. 9D. (For interpretation of the references to colour in this figure legend, the reader is referred to the Web version of this article.)

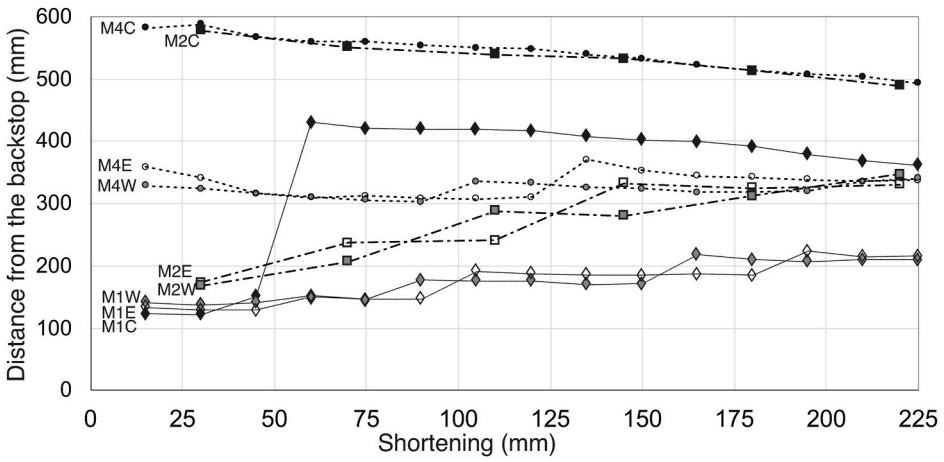

Fig. 11. Graphical plot illustrating the distance of the deformation front with respect to the backstop versus cumulative shortening. To enhance clarity, only the three most representative models are included in the plot. The discrepancy between model 1 and models 2 and 4 at early stages of shortening arises from the larger distance between the back edge of the silicon trapezium and the backstop (see Fig. 2A). In all models, the distance of the thrust front in the viscous domain retreated towards the backstop, while the thrust front in the frictional domain advanced. Consequently, the distance between both fronts decreased with increasing shortening, gradually reducing the prominence of the salient. Each data point on the plot represents a measurement of the deformation front taken along cross sections of the scanned top surfaces of the models. See locations across the models in Fig. 12.

domain, both the thrust front and the thrust nucleated over the step between the silicone layers were active, along with thrusts near the backstop (Fig. 12). Subsequently, upon reaching the critical height of the wedge, the thrust wedges above the frictional detachment advanced forward through the successive accretion of new thrusts, with limited internal deformation through synchronous thrusting. Simultaneously, the thrust wedge above the viscous detachment retreated in relation to the backstop and underwent primarily internal deformation, characterized by imbrication and out-of-sequence thrusts at the frontal parts of the wedge where the sand package above the silicone was thinner (Figs. 3–10 and 12).

The occurrence of out-of-sequence thrusts and the backward propagation of the deformation into thrust wedges above a viscous detachment were consistent with findings in prior analogue modelling experiments (Cotton and Koyi, 2000; Costa and Vendeville, 2002; Li and Mitra, 2017; Borderie et al., 2018). In experiments involving a constant-thickness sand package above the viscous detachment, the thrust front migrated forward, but farther and faster compared to the adjacent frictional domains (Cotton and Koyi, 2000; Costa and Vendeville, 2002; Luján et al., 2003; Li and Mitra, 2017; Werf et al., 2023). Consequently, the deformation front advanced incrementally at an increasingly greater distance during the formation of a new frontal thrust, before the pinch-out of the silicone was reached (see distance of the deformation front/shortening plots in Cotton and Koyi, 2000; Luján et al., 2003; Li and Mitra, 2017). In contrast, experiments featuring an initial sand wedge thickening toward the backstop facilitated rapid forward migration of the deformation to the silicone pinch-out and intensified the backward internal deformation of the thrust wedge as shortening persisted (Smit et al., 2003; and our experiments). As a result, the thrust front of the viscous domain gradually retreated in our model results (Figs. 11 and 12). Consequently, the distance between the thrust fronts in the viscous and adjacent frictional domains decreased, and the thrust salient progressively became less pronounced (Figs. 11–13).

The interaction between structures in different domains depended on the geometry of the viscous detachment and the distance between active structures. Models with a lateral edge of the silicone trapezium forming an internal angle with the backstop trend greater than 90°, leaving a frictional area between the backstop and the lateral silicone edge along the shortening direction, illustrated such interaction (Fig. 2A, 3 and 5, and 7). With this configuration, the SW corner of the viscous detachment was not activated initially as deformation jumped to its forward edge farther east. The triangular frictional area of the transitional domain between the NE-SW silicone edge and the western frictional wedge buffered the propagation of deformation (Fig. 7). This SW corner of the viscous detachment progressively activated as new thrusts propagated ahead of the western frictional wedge. Each of these thrusts curved toward the western edge of the silicone, forming N–S to NW-SE trending folds and thrusts highly oblique to, and plunging toward, the lateral silicone edge (Fig. 13). At the same time, the southern viscous frontal structure propagated to the west, also curving to form a system of N–S to NW-SE trending folds plunging toward the western edge of the silicone and connecting with coeval structures in the frictional thrust wedge (Fig. 13). The intersection of the two sets of plunging structures formed a structural depression near, but aligned slightly oblique to, the edge of the viscous detachment (Fig. 13). The oblique to lateral structures were best developed when the angle between the oblique edge of the silicone polygon and the shortening direction was 45° (Fig. 5). The trend of these oblique structures was modified by clockwise vertical-axis rotation related to the divergent displacement pattern of the sand wedge above the viscous detachment as recorded by lines tracking sand grains during the experiments (Fig. 13). Divergent displacement vectors have already been reported in previous studies modelling thrust salients above viscous detachments (Bahroudi and Koyi, 2003).

The step joining the two silicone layers of the viscous detachment, reproducing an inherited extensional fault, nucleated a thrust with minor displacement. This developed primarily close to the lateral edges of the silicone polygon that formed internal angles of <90° with the backstop trend (eastern sides of Figs. 5 and 7 and both sides of Fig. 9; see Fig. 13). This structure interacted with a newly formed thrust in the adjacent frictional detachment, changing its orientation in the transitional domain and increasing the spacing with respect to the previous thrust front (Figs. 5, 7, 9 and 13). The asymmetry of the trapezium also controlled the plunge of this structure, which in models 4 and 5 was westwards (Figs. 5, 7 and 13).

During the late stages of the experiments, the initial frontal thrust of the viscous domain significantly reduced or even ceased growth, as shown by the unconformity at the bottom of the sand sourced from the active thrust front (Figs. 10 and 12). At that point, internal deformation of the thrust wedge above the viscous detachment was accommodated mainly by out-of-sequence stacking of thrust sheets involving the thinner external parts of the sand wedge (Figs. 6, 8, 10 and 12). This was an unexpected result, as such a thrust sequence is known to be enhanced by synorogenic sedimentation, as observed in the field and demonstrated by numerical and analogue experiments (Vergés and Muñoz,

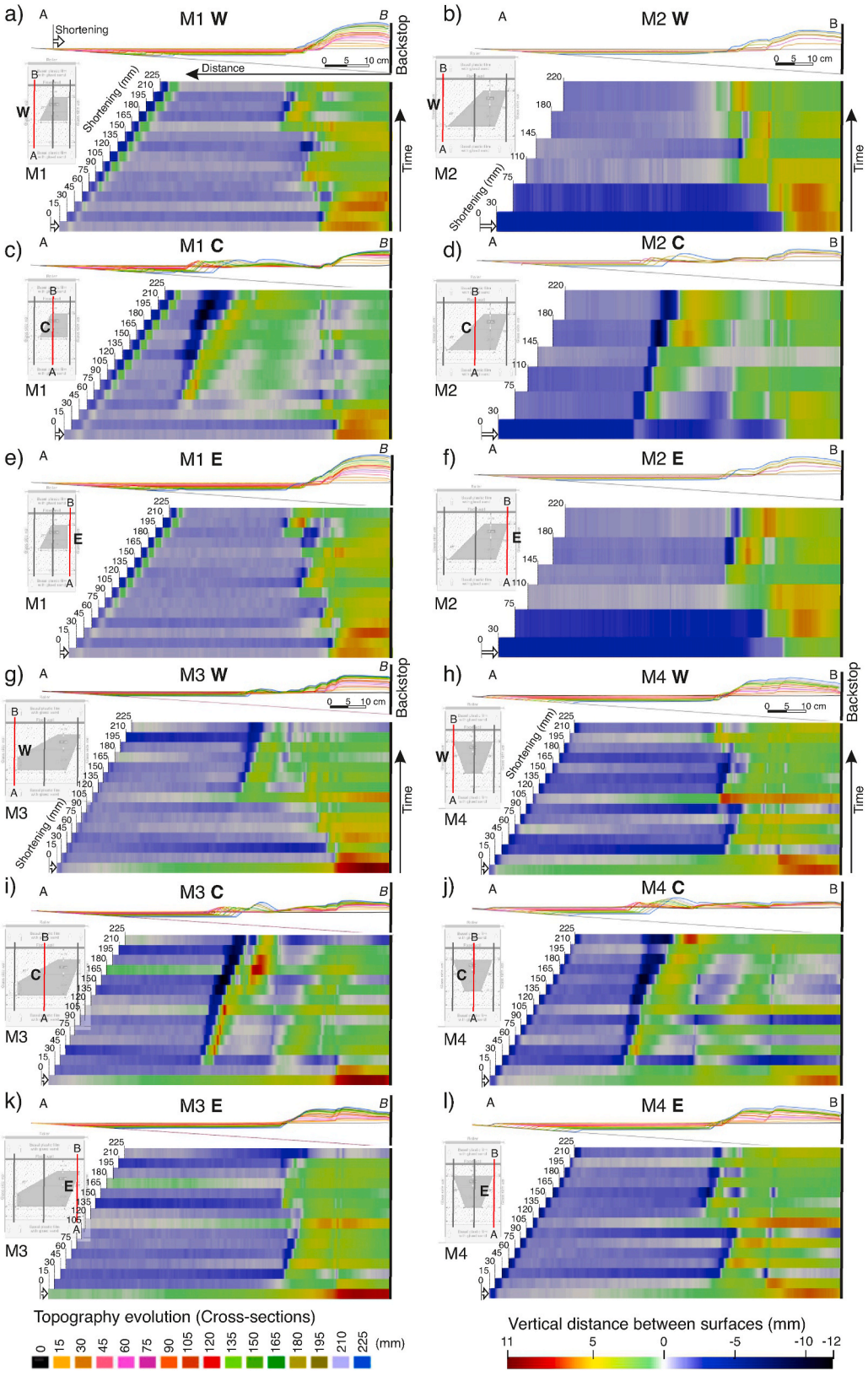

Fig. 12. Topographic evolution for three representative cross sections across the frictional and viscous domains of each model (locations shown in insets of each panel). The surface topography of the models was documented at every 2 cm of shortening utilizing a submillimeter-resolution white light scanner (*SidioPro* from *Nub3D*). For each panel showing one cross section, the profiles at the top depict the evolution of topography (bottom left scale) and the main part of the panel illustrates the incremental change in elevation with increasing shortening (bottom to top; scale in lower right of figure). This plot provides a visual representation of the distribution of deformation for each time interval.

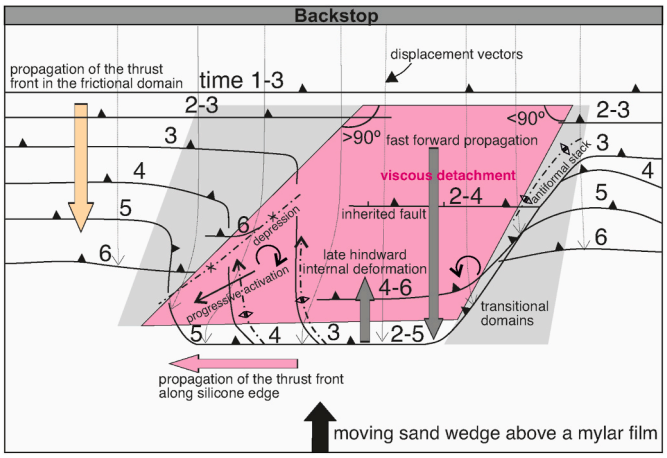

Fig. 13. Sketch illustrating a summary of the modelling results. It shows the asymmetry of the structural evolution controlled by the geometry of the viscous detachment, with a particular emphasis on the angle of the lateral oblique edges of the silicone trapezium in relation to the shortening direction. Notably, there is a sharp distinction between the western side, characterized by an upper (northern) internal angle of the trapezium greater than 90°, and the eastern side, where this angle is smaller than 90°. The numbers in the sketch denote a temporal sequence of deformation. Displacement vectors (thin grey lines with arrows) were determined by tracking sand scratches from the sequence of overhead images. See text for explanation.

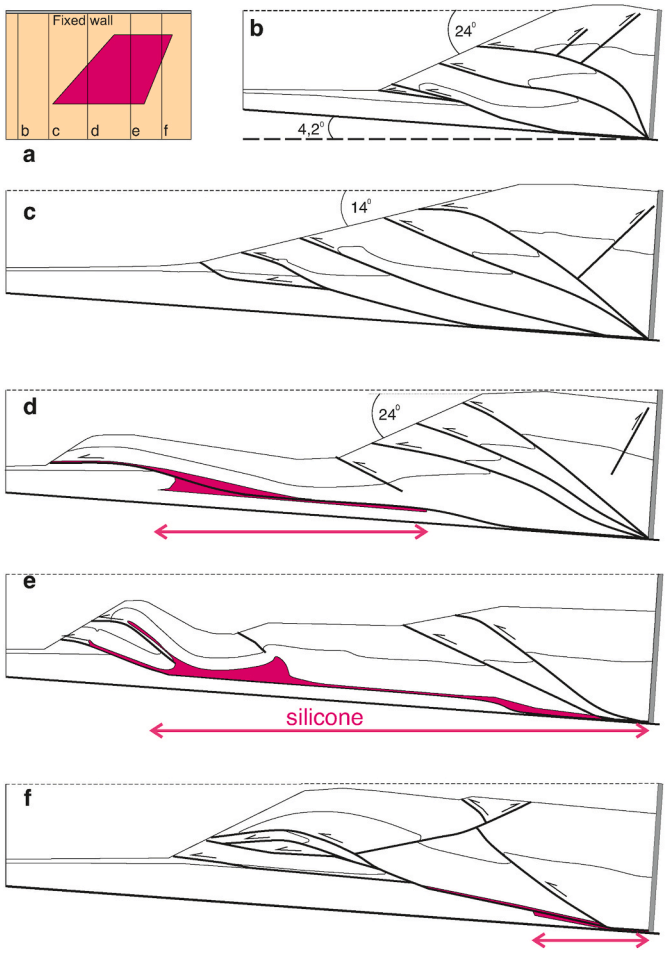

Fig. 14. Simplified sections across representative selected areas of the models showing the structural topography and the variation of the surface taper according to the position with respect to the viscous detachment with a trapezium geometry (location shown in A). Similarly to Fig. 13, these sections do not precisely correspond to specific cross-sections of the models but aim to summarize and illustrate the main structural features and surface taper observed in the model experiments.

1990; Fillon et al., 2013; Pla et al., 2019). Thus, more realistic experiments including syntectonic sedimentation would most probably enhance the internal deformation of the thrust wedge, not only above the viscous detachment by a break-back thrust sequence, but also within the adjacent frictional wedges. During the last stages of shortening, active structures aligned approximately along strike. The thrust fronts of the frictional domains connected across the oblique structures of the lateral edges of the silicone trapezium with the most active thrust inside the thrust wedge of the viscous domain (Figs. 3, 5, 7 and 9; structure 6 of Fig. 13).

The absence of erosion during the experiments did not promote the formation of silicone diapirs. However, two small diapirs formed during the experiments, both related to slumping of sand in the frontal structures (Figs. 3 and 9).

5.2. Surface topography

The final surface elevation in all experiments revealed higher topography and a narrower wedge above the frictional detachments, in contrast to lower topography and a wider wedge above the viscous detachment, aligning with predictions from Coulomb taper theory (Davis et al., 1983). This pattern has been consistently illustrated in numerous analogue and numerical modelling studies (Costa and Vendeville, 2002; Bahroudi and Koyi, 2003; Hardy et al., 2009; Graveleau et al., 2012; Vendeville et al., 2017) (Fig. 14). Nevertheless, there were some differences observed among the models that are not fully predicted by Coulomb taper theory.

It is worth noting that in analogue experiments, the topography of the thrust wedge is influenced by various factors, including the height and geometry of the backstop. Consequently, taper angles vary significantly among different experiments, and their comparison with natural examples is not straightforward (see reviews by Buiter, 2012; Graveleau et al., 2012). Despite these challenges, the evolution of surface topography remains a valuable parameter for comparing different experiments.

The surface taper in the frictional domain, away from the influence of the viscous detachment, was characterized by a high angle, of about 24°. (Fig. 14b). However, in the transitional area between the frictional detachment and the viscous detachment, the thrusts curved to connect with the active frontal structures at the forward edge of the viscous detachment (Fig. 13). Consequently, the distance to the thrust front increased in the transitional area, leading to a reduction in surface taper even though the wedge did not involve the silicone layer along sections parallel to the shortening direction (Fig. 14c; compare Figs. 3B, 5B and 8A). In this area, surface topography was not governed by thrust wedge mechanics (i.e. the critical taper theory) but by thrust kinematics. Similar relationships have been proposed by Li and Mitra (2017). Despite the lower taper, the elevation of the sand wedge was the same and was the highest among all the models (Fig. 14).

The taper of the thrust wedge involving the viscous detachment depended on the position of the silicone layer with respect to the backstop along cross-sections parallel to the transport direction (Fig. 14). In the sections across a lateral edge of the silicone trapezium displaying an internal angle with the backstop edge greater than 90°, the final surface taper geometry consisted of two distinct juxtaposed wedges (Fig. 14d). The internal wedge above the rear frictional detachment, showed the same surface taper angle (24°) as the frictional thrust wedge away from the influence of the viscous detachment (Fig. 14b and d). In the adjacent external wedge, developed above the viscous domain, the surface taper decreased to horizontal or even negative values (Fig. 14d). The final topography is significantly less than in the previous models.

Similar taper values of composite wedges have been described in experiments involving a rear frictional domain between the backstop and the viscous domain (Luján et al., 2003; Li and Mitra, 2017).

A section across the entire viscous detachment showed the lowest height and surface taper, in accordance with the predictions of Coulomb taper theory (Fig. 14e and supplementary animations S1–S4). However, three discrete parts can be distinguished. In the internal part, the topography increased as the sand wedge behind the silicone polygon started to deform. The critical maximum height was less than in other areas because deformation propagated forward since the initial stages. The thrust wedge located above the viscous detachment displayed a horizontal surface taper above a mostly undeformed sand pack. Finally, the frontal wedge showed the maximum height, acquired through internal deformation during the last stages of deformation (Figs. 1 and 5–7 and 94e).

Finally, sections across the internal corners of the silicone polygons, across lateral edges of the trapezium showing an internal angle with the backstop base smaller than 90°, exhibited a distinct structural style and surface taper (Fig. 14f). In such sections, even though the width of the involved viscous detachment was small and restricted to the internal part, the surface had a negative angle, subparallel to the basal angle. The highest topography was observed in the frontal structure, which is related to the oblique antiformal stack developed along the lateral edges of the viscous detachment, as explained in the previous section (Fig. 6f, 9e and 10 and 12f).

These topographic differences may have a significant impact on the sedimentary routing system of synorogenic sediments as will be discussed below.

5.3. Comparison with the central South-Pyrenean Thrust Salient

The experimental results of this study are consistent with the main features of the South-Central Pyrenean Thrust Salient. Importantly, they provide new ideas for the interpretation of the available surface and subsurface data. In addition, they bring new insights to the understanding of other salt-detached fold-and-thrust belts, such as the Jura Mountains, Zagros or South-Western Alps.

The Triassic salt distribution at the base of the South Pyrenean thrust sheets, inherited from pre-orogenic tectonic events, has been inferred through a combination of surface and subsurface data sets (Muñoz et al., 2013, 2018). We reproduced this distribution with a scalene trapezium geometry in models 2 and 3, where the lateral edges trend SW-NE - the western edge formed an internal angle greater than 90° with the backstop edge of the trapezium, while the eastern edge formed an angle smaller than 90°, (setup Fig. 2A and 13). This geometric arrangement served to elucidate the observed asymmetry and structural evolution in the South-Central Pyrenean Thrust Salient. Moreover, the deformation and interaction of the viscous and brittle thrust wedges, and the

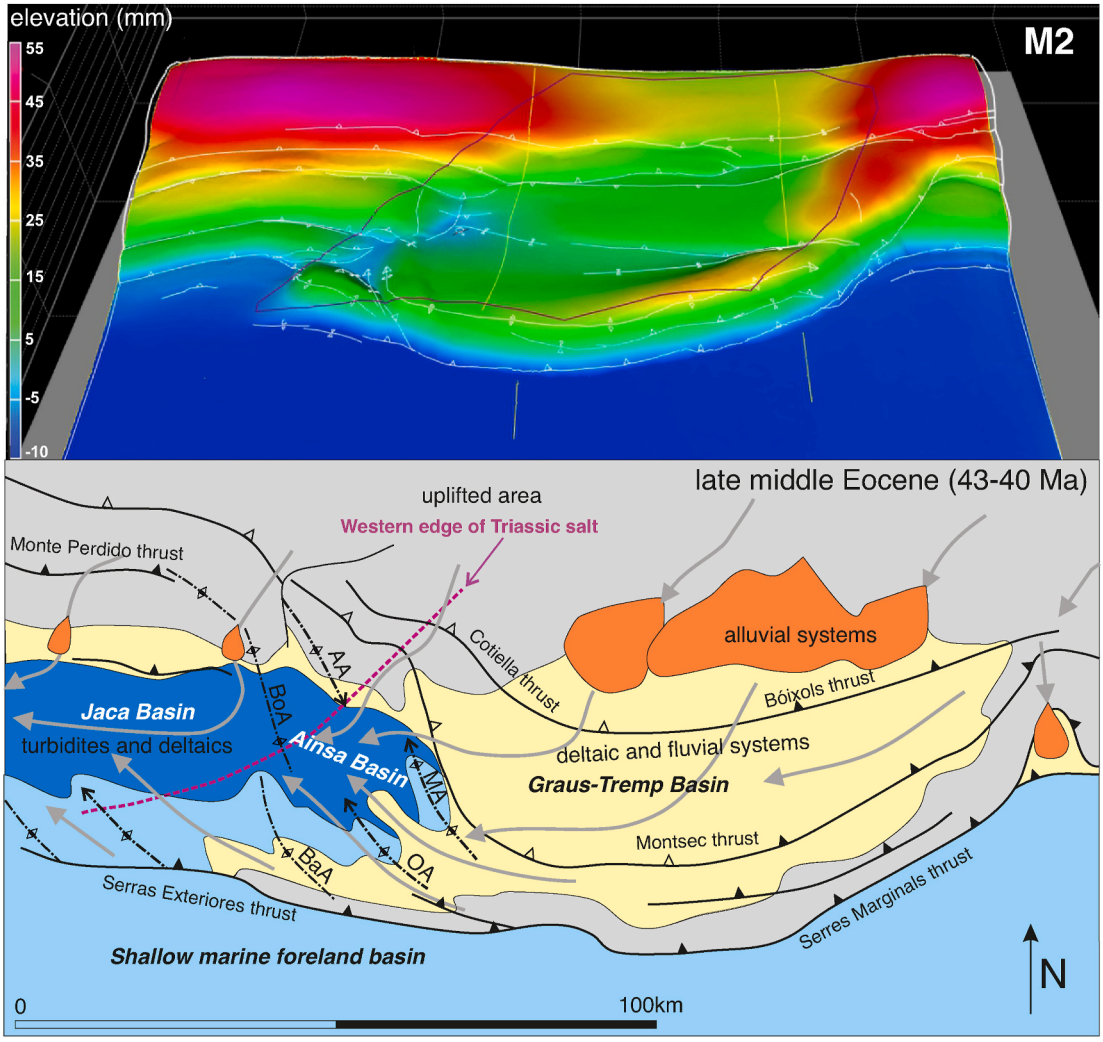

Fig. 15. Oblique view showing the topography of Model 2 (top) and comparison with the paleogeographic reconstruction of the South-Central Pyrenean Thrust Salient at late middle Eocene times (bottom, based on the reconstruction by Garcés et al., 2020).

consequent surface topography, also illustrated the main tectono-stratigraphic features observed in the piggy-back basins, including the distribution and routing of synorogenic sediments (Fig. 15).

According to our modelling results, the South-Central Pyrenean Thrust Salient can be interpreted as a progressive curvature with a divergent thrust displacement (Muñoz et al., 2013). However, in the models, structures were only slightly curved during deformation, and the observed obliquity mainly resulted from either the connection of active structures in the frictional and viscous domains across transitional areas at a given time or the activation of the oblique silicone edges if properly oriented (Fig. 13). In both cases, the final orientation of the oblique structures did not coincide with the original orientation of the lateral edges of the viscous detachment.

The Ainsa Oblique Zone, in the western part of the South-Central Pyrenean Thrust Salient, is characterized by N–S trending folds that grew during the middle to late Eocene late stages of the Ainsa Basin infill (Muñoz et al., 2013). In the southern part of the basin, these folds are salt-cored detachment anticlines. They show a prominent northward plunge and propagated westward along the Sierras Exteriores thrust front (Figs. 1 and 15) (Millán et al., 2000; Mochales et al., 2012; Rodriguez-Pintó et al., 2016). In the northern part of the basin, folds mainly plunge southwards, and they show a different style with fault-propagation fold geometries curving westwards into the WNW-ESE Pyrenean trend (Figs. 1 and 15). The structural depression between both sets of structures (Ainsa-Jaca basins) was controlled by the location of the oblique edge of the Triassic salt and localized the turbiditic systems sourced from proximal sediments located further east (Fig. 15). All these features have been reproduced in our experiments, in the transitional areas along the lateral edges of the viscous detachment with a northern internal angle of the trapezium greater than 90°, oblique to the shortening direction (models 1, 2 and 3; Figs. 5, 7, 13 and 15). The N–S trending structures of the Ainsa Oblique Zone have also been recently studied using analogue models (Werf et al., 2023). These authors illustrated in their model results the formation of oblique structures along the transitional area between frictional and viscous domains. However, their model, with a setup characterized by a lateral edge of the viscous detachment parallel to the shortening direction, did not reproduce the structural depression along the silicone edge and all the related structural features.

One significant difference between observations and model results is the recorded amount of vertical-axis rotation during westward propagation of the deformation along the viscous thrust front. This rotation is up to 55°-70° in the Boltaña and Mediano anticlines (Mochales et al., 2012; Muñoz et al., 2013) but only up to 36° in our models (Figs. 3, 5 and 7). Werf et al. (2023) also obtained a similar value of clockwise vertical-axis rotation in their model.

The eastern edge of the South-Central Pyrenean Thrust Salient can also be explained by a viscous detachment with an original SW-NE trending oblique lateral edge, but with a northern internal angle of the silicone trapezium smaller than 90° (Figs. 13 and 15). This initial inherited geometry would explain the higher structural elevation in the eastern part of the South-Central Pyrenean Thrust Salient provided by the westward plunge of the frontal and internal structures developed during earlier and faster activation above the eastern part of the viscous detachment (Figs. 4, 7 and 13). The eastern oblique structures in the models experienced less VAR than the western oblique structures, as also recorded in nature (Fig. 13, Sussman et al., 2004; Muñoz et al., 2013). The final orientation of the eastern oblique structures in the models differed from the initial orientation of the silicone edge by as much as 30° (Figs. 5, 7 and 9).

The thrust sequence and internal deformation of the thrust wedge above the viscous detachment in the central and frontal parts of the thrust salient were also consistent with the observations made in our natural prototype, despite the absence of synorogenic sedimentation in the experimental program. This frontal part was characterized by hindward-migrating internal deformation, with the development of synchronous thrusts and related tight folds and out-of-sequence thrusts. This structural style resulted from a thin mechanical stratigraphy above the viscous detachment and resembled the structures observed along the entire front of the South-Central Pyrenean Thrust Salient (Figs. 1, 6, 9 and 10) (Millán et al., 2000; Muñoz et al., 2018).

The top views of the models exhibited antiformal geometries that could be interpreted as structures related to salt inflation, as there was no clear surface evidence of thrust imbrication. However, sections across these antiforms revealed thrust repetitions of the thin stratigraphic units (i.e., Fig. 10). In the eastern part of the South-Central Pyrenean Thrust Salient, the relief of frontal structures, such as the Sant Mamet antiform (Fig. 1), have been explained by either thrust imbrication (Muñoz et al., 2018) or salt inflation (Séguret, 1972; Burrel and Teixell, 2021). Model results, along with the observed out-of-sequence thrusts enhanced by synorogenic sedimentation in the external parts of the Serres Marginals thrust sheet and Sierras Exteriores (Vergés and Muñoz, 1990) would support the thrust-imbrication hypothesis. Internal deformation of the thrust front above the viscous detachment would also explain the absence of stratigraphic record in the Serres Marginals thrust sheet at the frontal parts of the South-Central Pyrenean Thrust Salient during the middle Eocene (Fig. 15). This frontal part would have experienced uplift once the adjacent frictional thrust wedges advanced forward, connecting and interacting with the internal structures of the viscous thrust wedge (Figs. 13–15).

The final surface topography of the models, which was controlled by the geometry of the viscous detachment, also aligns with the distribution and dispersal pattern of the synorogenic sediments preserved in the piggy-back and foreland basins of the South-Central Pyrenees (Figs. 14 and 15). The smaller surface taper and lower topography of the wedge above the central part of the viscous detachment explains the preservation of the proximal parts of the synorogenic sediments in the South-Central Pyrenean Thrust Salient, represented by alluvial fans (Beamud et al., 2011; Vincent, 1999). These proximal sediments were sourced from the adjacent uplifted areas and graded laterally (westward) into fluvio-deltaic sediments and the coeval slope systems of the Ainsa-Jaca basins (Fig. 15). According to the models, the transition to deeper sediments coincides approximately with the structural depression initially located along the oblique western boundary of the viscous detachment, although it was progressively transported forward while also changing its orientation slightly (Fig. 15). A significant result of the experiments is the difference in structural relief between the two oblique lateral edges of the silicone trapezium (Fig. 15). The eastern oblique edge experienced uplift since the early stages, while the western one was characterized by a structural depression.

In summary, the South-Central Pyrenean Thrust Salient can be considered as a combination of a progressive curvature with a primary influence. It is not a primary arch because the oblique structures are not parallel to the inherited edges of the Upper Triassic salt detachment. The oblique structures may form at a high angle to the salt edge (in cases of a lateral edge of the silicone trapezium with a northern internal angle greater than 90°) or a moderate to small angle (lateral edge of the silicone trapezium with a northern internal angle smaller than 90°, Fig. 13).

6. Conclusions

The experimental program presented in this work suggests that the South-Central Pyrenean Thrust Salient can be interpreted as a result of the contractional deformation of the Jurassic-Cretaceous sediments above a Triassic salt layer showing an initial inherited trapezium geometry widening forward, with lateral edges trending SW-NE. The wedge geometry of the suprasalt Mesozoic succession in the South-Central Pyrenees, marked by a northward increase in thickness, facilitated the forward propagation of contractional deformation above the viscous Triassic detachment since the early stages. This fast propagation triggered the activation of the salt pinch-out and promoted the

development of the oblique structures along the lateral edges of the salt basin.

Our modelling results demonstrate that none of the oblique structures exhibited the same orientation as the lateral edges of the viscous layer that caused them to form. The angle between the suprasalt structures and the edge of the detachment depended on the internal angle of the silicone polygon near the backstop. When this angle exceeded 90°, a frictional transitional area was positioned at the rear of the viscous domain (Fig. 13). In such a configuration, oblique structures within the transitional area between frictional and viscous domains formed at a high angle to the lateral edge of the viscous detachment. Additionally, a structural depression developed along this lateral edge as the structures above the western frictional detachment curved and linked with the active structures at the thrust front of the viscous domain located toward the foreland. These features are entirely consistent with observations in the Ainsa Oblique Zone, at the western part of the South-Central Pyrenean Thrust Salient (Figs. 13 and 15).

The observed asymmetry of the South-Central Pyrenean Thrust Salient can be attributed to the uneven distribution of the Triassic evaporites. In our experiments, we replicated this asymmetry through the eastern lateral edge of the silicone trapezium, forming an internal angle smaller than 90° with the trend of the backstop. In this scenario, and in contrast to the western lateral edge, the transitional area with the frictional domain is located in front of the silicone (Fig. 13). An oblique thrust developed along this edge, evolving into an antiformal stack slightly oblique to the initial orientation of the silicone edge. These features, along with the westward plunge of the main folds, are also consistent with the characteristics of the eastern edge of the South-Central Pyrenean Thrust Salient (Figs. 13 and 15).

Thrust kinematics differ in the thrust wedges developing above frictional and viscous detachments. In the frictional domains, the thrust sequence evolved from synchronous thrusting to forward propagation in the absence of syntectonic sedimentation. On the contrary, the thrust wedge above the viscous detachment deformed internally by a break-back thrust sequence once the adjacent and internal frictional wedges acquired a critical height to advance forwards. Out-of-sequence thrusts in the viscous domain interacted and connected with the progressively new-formed thrusts in the adjacent frictional domains along the transitional domain, where oblique structures formed. A consequence of this contrasting kinematics in the different domains is that the thrust salient depicted by the active structures was initially larger and decreased in prominence as deformation progressed. All these kinematic relationships described from the experimental results are also observed in the South-Central Pyrenean Thrust Salient.

The surface taper angle and the related topography showed higher values in the frictional domains than in the viscous domain. However, the taper also exhibited significant variations along strike, depending on the orientation of the oblique lateral edges of the viscous detachment. In cross sections across the lateral edges with a frictional transitional area behind (internal angle of the silicone trapezium greater than 90°), the final thrust wedge comprised two juxtaposed wedges: the internal one with a steeper angle and the external one with a horizontal to negative angle (Fig. 14). The lowest topography was situated at the boundary between these two wedges, initially positioned along the oblique edge of the viscous detachment. In contrast, sections across oblique lateral edges with the frictional transitional area forward of the silicone showed a surface taper characterized by negative values, with the highest relief located at the frontal antiformal stack. Sections across frictional transitional areas displayed a smaller surface taper compared to adjacent frictional domains (Fig. 14). The final topography observed in the models nicely explains the main paleogeographic reconstructions interpreted in the South-Central Pyrenean Thrust Salient, including the location of the Ainsa Basin and the westward sediment transport into the low.

In summary, the structures that evolved in the frictional and viscous domains interacted with each other, leading to modifications in their location, spacing, orientation, kinematics, and surface taper, particularly in the transitional areas. This interaction depended on the geometry of the viscous detachment. These results should be considered when interpreting the observed geometry and original configuration of salt-detached fold-and-thrust belts. Often, there is a tendency to interpret the observed oblique structures as reproducing the initial edges of the salt layer, regardless of their nature (fault or pinch-out). The results from the models and the structures observed in the South-Central Pyrenean Thrust Salient highlight that, in cases involving an unevenly distributed salt layer, most oblique structures show different geometries and orientations. In general, they do not necessarily mimic the original limits of the salt detachment.

CRediT authorship contribution statement

Josep A. Muñoz: Writing – review & editing, Writing – original draft, Supervision, Investigation, Funding acquisition, Conceptualization. **Oriol Ferrer:** Writing – original draft, Methodology, Formal analysis. **Oscar Gratacós:** Visualization, Methodology, Investigation, Formal analysis, Conceptualization. **Eduard Roca:** Supervision, Project administration, Funding acquisition, Conceptualization.

Declaration of generative AI and AI-assisted technologies in the writing process

During the preparation of the final version of this manuscript the authors used ChatGPT in order to improve language and readability of some paragraphs of the original draft of the manuscript. After using this tool, the authors reviewed and edited the content as needed and take full responsibility for the content of the publication.

Declaration of competing interest

The authors declare the following financial interests/personal relationships which may be considered as potential competing interestsJosep Anton Muñoz reports financial support provided by Ministerio de Ciencia e Innovación (Gobierno de España). Oriol Ferrer reports financial support was provided by Ministerio de Ciencia e Innovación (Gobierno de España).

Data availability

Data will be made available on request.

Acknowledgements

This article is dedicated to Bruno Vendeville, in recognition of his valuable contribution to the understanding of salt tectonics. We acknowledge the support of the research project Structure and Deformation of Salt-bearing Rifted Margins (SABREM), PID2020-117598 GB-I00, funded by MCIN/AEI/10.13039/501100011033, and the VIG-EOOCULT (PLEC2021-007903) and GEODIGIT (TED2021-130602B–I00) research projects funded by MCIN/AEI/10.13039/501100011033 and for the European Union "NextGenerationEU"/PRTR.

The GEOMODELS Research Institute and the Grup de Geodinàmica i Anàlisi de Conques (2021SGR76) are also acknowledged for their financial support. We also thank Maria Roma, Oriol Pla, Frederic Escosa and Genís Nin for logistical support in the modelling laboratory. Petex and Aspentech are thanked for providing academic licenses for Move and GoCad software, respectively.

The authors express gratitude to Ian Alsop and Mark Rowan for the editorial handling of the manuscript. Special thanks are extended to Fabien Graveleau (Guest Editor) and Fabrizio Storti for their detailed reading and constructive comments, that have improved the original draft of this paper. The authors would also like to acknowledge the

comments provided by an anonymous reviewer, contributing to the strengthening of the manuscript's content. Furthermore, gratitude is expressed for the corrections and contributions made by Mark Rowan and Pablo Santolaria.

Appendix A. Supplementary data

Supplementary data to this article can be found online at https://doi.org/10.1016/j.jsg.2024.105078.

References

Alonso, J., Pulgar, J., García-Ramos, J., Barba, P., 1996. W5 tertiary basins and alpine tectonics in the cantabrian mountains (NW Spain). In: Friend, P.F., Dario, C.J. (Eds.), Tertiary Basins of Spain, Tertiary Basins of Spain. Tertiary basins of Spain, pp. 214–227.

Bahroudi, A., Koyi, H., 2003. Effect of spatial distribution of Hormuz salt on deformation style in the Zagros fold and thrust belt: an analogue modelling approach. J. Geol. Soc. 160, 719–733. https://doi.org/10.1144/0016-764902-135.

Beamud, E., Muñoz, J.A., Fitzgerald, P.G., Baldwin, S.L., Garcés, M., Cabrera, L., Metcalf, J.R., 2011. Magnetostratigraphy and detrital apatite fission track thermochronology in syntectonic conglomerates: constraints on the exhumation of the South-Central Pyrenees. Basin Res. 23, 309–331.

Beaumont, C., Muñoz, J.A., Hamilton, J., Fullsack, P., 2000. Factors controlling the Alpine evolution of the central Pyrenees inferred from a comparison of observations and geodynamical models. J. Geophys. Res. Solid Earth 105 (1978–2012), 8121–8145.

Becker, A., 2000. The Jura Mountains — an active foreland fold-and-thrust belt? Tectonophysics 321, 381–406. https://doi.org/10.1016/s0040-1951(00)00089-5.

Berastegui, X., García-Senz, J., Losantos, M., 1990. Tecto-sedimentary evolution of the Organyà extensional basin (central south Pyrenean unit, Spain) during the Lower Cretaceous. Bullet. Soc. Géol. France 2, 251–264. https://doi.org/10.2113/gssgfbull.vi.2.251.

Borderie, S., Graveleau, F., Witt, C., Vendeville, B.C., 2018. Impact of an interbedded viscous décollement on the structural and kinematic coupling in fold-and-thrust belts: insights from analogue modeling. Tectonophysics 722, 118–137. https://doi.org/10.1016/j.tecto.2017.10.019.

Buiter, S.J.H., 2012. A review of brittle compressional wedge models. Tectonophysics 530, 1–17. https://doi.org/10.1016/j.tecto.2011.12.018.

Burrel, L., Teixell, A., 2021. Contractional salt tectonics and role of pre-existing diapiric structures in the Southern Pyrenean foreland fold–thrust belt (Montsec and Serres Marginals). J. Geol. Soc. 178 (4) https://doi.org/10.6084/m9.figshare.c.5287737.

Callot, J.P., Jahani, S., Letouzey, J., 2007. The role of pre-existing diapirs in fold and thrust development. In: Lacombe, O., Lavé, J., Roure, F., Vergés, J. (Eds.), Thrust Belts and Foreland Basins, from Fold Kinematics to Hydrocarbon Systems. Springer, Frontiers in Earth Sciences, Berlin, pp. 309–325. https://doi.org/10.1007/978-3-540-69426-7_16.

Callot, J.P., Trocmé, V., Letouzey, J., Albouy, E., Jahani, S., Sherkati, S., 2012. Pre-existing salt structures and the folding of the Zagros Mountains. In: Alsop, G.I., Archer, S.G., Hartley, A.J., Grant, N.T., Hodgkinson, R. (Eds.), Salt Tectonics, Sediments and Prospectivity, vol. 363. Geological Society, London, Special Publications, pp. 545–561. https://doi.org/10.1144/sp363.27.

Cámara, P., 2020. Inverted turtle salt anticlines in the Eastern Basque-Cantabrian basin, Spain. Mar. Petrol. Geol. 117, 104358 https://doi.org/10.1016/j.marpetgeo.2020.104358.

Célini, N., Callot, J.-P., Ringenbach, J.-C., Graham, R., 2020. Jurassic salt tectonics in the SW sub-alpine fold-and-thrust belt. Tectonics 39. https://doi.org/10.1029/2020tc006107, 47–36.

Cofrade, G., Závada, P., Krýza, O., Cantarero, I., Gratacós, Ò., Ferrer, O., Adineh, S., Ramirez-Perez, P., Roca, E., Travé, A., 2023. The kinematics of a salt sheet recorded in an array of distorted intrasalt stringers (Les Avellanes Diapir – South-Central Pyrenees). J. Struct. Geol. 176, 104963. https://doi.org/10.1016/j.jsg.2023.104963.

Costa, E., Vendeville, B.C., 2002. Experimental insights on the geometry and kinematics of fold-and-thrust belts above weak, viscous evaporitic décollement. J. Struct. Geol. 24, 1729–1739.

Cotton, J.T., Koyi, H.A., 2000. Modeling of thrust fronts above ductile and frictional detachments: application to structures in the Salt Range and Potwar Plateau, Pakistan. GSA Bulletin 112, 351–363. https://doi.org/10.1130/0016-7606(2000)112<;351:motfad>2.0.co;2.

Davis, D.M., Engelder, T., 1985. The role of salt in fold-and-thrust belts. Tectonophysics 119, 67–88. https://doi.org/10.1016/0040-1951(85)90033-2.

Davis, D., Suppe, J., Dahlen, F.A., 1983. Mechanics of fold-and-thrust belts and accretionary wedges. J. Geophys. Res. Solid Earth 88 (1978–2012), 1153–1172. https://doi.org/10.1029/jb088ib02p01153.

Davy, P., Cobbold, P.R., 1988. Indentation Tectonics in Nature and Experiment, 1. Experiments Scaled for Gravity, vol. 14. Bulletin of the Geological Institutions of the University of Uppsala, pp. 129–141 new series.

Dell'Ertolle, D., Schellart, W.P., 2013. The development of sheath folds in viscously stratified materials in simple shear conditions: an analogue approach. J. Struct. Geol. 56, 129–141. https://doi.org/10.1016/j.jsg.2013.09.002.

Dinarès, J., McClelland, E., Santanach, P., 1992. Contrasting rotations within thrust sheets and kinematics of thrust tectonics as derived from palaeomagnetic data: an example from the Southern Pyrenees. In: McClay, K.R. (Ed.), Thrust Tectonics. Chapman and Hall, London, p. 265.

Duffy, O.B., Dooley, T.P., Hudec, M.R., Jackson, M.P.A., Fernandez, N., Jackson, C.A.-L., Soto, J.I., 2018. Structural evolution of salt-influenced fold-and-thrust belts_ A synthesis and new insights from basins containing isolated salt diapirs. J. Struct. Geol. 114, 206–221. https://doi.org/10.1016/j.jsg.2018.06.024.

Fernández, O., Muñoz, J.A., Arbues, P., Falivene, O., 2012. 3D structure and evolution of an oblique system of relaying folds: the Ainsa basin (Spanish Pyrenees). J. Geol. Soc. 169, 545–559.

Ferrer, O., Gratacós, O., Roca, E., Muñoz, J.A., 2017. Modeling the interaction between presalt seamounts and gravitational failure in salt-bearing passive margins: the Messinian case in the northwestern Mediterranean Basin. Interpretation 5, SD99–SD117. https://doi.org/10.1190/int-2016-0096.1.

Fillon, C., Huismans, R.S., Beek, P. van der, Muñoz, J.A., 2013. Syntectonic sedimentation controls on the evolution of the southern Pyrenean fold-and-thrust belt: inferences from coupled tectonic-surface processes models. J. Geophys. Res. Solid Earth 118, 5665–5680. https://doi.org/10.1002/jgrb.50368.

Fischer, M.P., Jackson, P.B., 1999. Stratigraphic controls on deformation patterns in fault-related folds: a detachment fold example from the Sierra Madre Oriental, northeast Mexico. J. Struct. Geol. 21, 613–633.

Garcés, M., Blanco, M.L., Valero, L., Beamud, E., Muñoz, J.A., Oliva-Urcía, B., Vinyoles, A., Arbués, P., Cabello, P., Cabrera, L., 2020. Paleogeographic and sedimentary evolution of the South Pyrenean foreland basin. Mar. Petrol. Geol. 113, 104105 https://doi.org/10.1016/j.marpetgeo.2019.104105.

Graveleau, F., Malavieille, J., Dominguez, S., 2012. Experimental modelling of orogenic wedges: a review. Tectonophysics 538–540, 1–66. https://doi.org/10.1016/j.tecto.2012.01.027.

Hardy, S., McClay, K., Muñoz, J.A., 2009. Deformation and fault activity in space and time in high-resolution numerical models of doubly vergent thrust wedges. Mar. Petrol. Geol. 26, 232–248. https://doi.org/10.1016/j.marpetgeo.2007.12.003.

Hubbert, M.K., 1937. Theory of scale models as applied to the study of geologic structures. GSA Bulletin 48, 1459–1520. https://doi.org/10.1130/GSAB-48-1459.

Huiqi, L., McClay, K.R., Powell, D., 1992. Physical models of thrust wedges. In: McClay, K.R. (Ed.), Thrust Tectonics. Chapman & Hall, London, pp. 71–81.

Jammes, S., Huismans, R.S., Muñoz, J.A., 2014. Lateral variation in structural style of mountain building: controls of rheological and rift inheritance. Terra. Nova 26, 201–207. https://doi.org/10.1111/ter.12087.

Jourdon, A., Mouthereau, F., Pourhiet, L.L., Callot, J.-P., 2020. Topographic and tectonic evolution of mountain belts controlled by salt thickness and rift architecture. Tectonics 39, 1–14. https://doi.org/10.1029/2019tc005903.

Koyi, H.A., Sans, M., Teixell, A., Cotton, J., Zeyen, H., 2004. The significance of penetrative strain in the restoration of shortened layers—insights from sand models and the Spanish Pyrenees. In: McClay, K.R. (Ed.), Thrust Tectonics and Hydrocarbon Systems, vol. 82. AAPG Memoir, pp. 207–222.

Larroque, C., Calassou, S., Malavieille, J., Chanier, F., 1995. Experimental modelling of forearc basin development during accretionary wedge growth. Basin Res. 7, 255–268. https://doi.org/10.1111/j.1365-2117.1995.tb00109.x.

Li, J., Mitra, S., 2017. Geometry and evolution of fold-thrust structures at the boundaries between frictional and ductile detachments. Mar. Petrol. Geol. 85, 16–34. https://doi.org/10.1016/j.marpetgeo.2017.04.011.

Lickorish, W.H., Ford, M., Bürgisser, J., Cobbold, P.R., 2002. Arcuate thrust systems in sandbox experiments: a comparison to the external arcs of the Western Alps. GSA Bulletin 114, 1089–1107. https://doi.org/10.1130/0016-7606(2002)114<;1089:atsise>2.0.co;2.

Lohrmann, J., Kukowski, N., Adam, J., Oncken, O., 2003. The impact of analogue material properties on the geometry, kinematics, and dynamics of convergent sand wedges. J. Struct. Geol. 25, 1691–1711. https://doi.org/10.1016/S0191-8141(03)00005-1.

López-Gómez, J., Alonso-Azcárate, J., Arche, A., Arribas, J., Fernández Barrenechea, J., Borruel-Abadía, V., Viseras, C., 2019. Permian-triassic rifting stage. In: Quesada, C., Oliveira, J.T. (Eds.), The Geology of Iberia: A Geodynamic Approach, vol. 3. Springer Nature Switzerland, pp. 29–112. https://doi.org/10.1007/978-3-030-11295-0_3. The Alpine Cycle. Regional Geology Reviews.

López-Mir, B., Muñoz, J.A., García-Senz, J., 2014. Extensional salt tectonics in the partially inverted Cotiella post-rift basin (south-central Pyrenees): structure and evolution. Int. J. Earth Sci. 104, 419–434. https://doi.org/10.1007/s00531-014-1091-9.

Luján, M., Storti, F., Balanyá, J.C., Blanc, A.C., Rossetti, F., 2003. Role of décollement material with different rheological properties in the structure of the Aljibe thrust imbricate (Flysch Trough, Gibraltar Arc): an analogue modelling approach. J. Struct. Geol. 25, 867–881.

Manatschal, G., Chenin, P., Lescoutre, R., Miró, J., Cadenas, P., Saspiturry, N., Masini, E., Chevrot, S., Ford, M., Jolivet, L., Mouthereau, F., Thinon, I., Issautier, B., Calassou, S., 2021. The role of inheritance in forming rifts and rifted margins and building collisional orogens: a Biscay-Pyrenean perspective. BSGF - Earth Sci. Bullet. 192, 55. https://doi.org/10.1051/bsgf/2021042.

Marshak, S., 2004. Salients, recesses, arcs, oroclines, and syntaxes – a review of ideas concerning the formation of map-view curves in fold thrust belts. In: McClay, K.R. (Ed.), Thrust Tectonics and Hydrocarbon Systems, vol. 82. AAPG Memoir, pp. 131–156.

Martín-Chivelet, J., Floquet, M., García-Senz, J., Callapez, P.M., López-Mir, B., Muñoz, J.A., et al., 2019. Late cretaceous post-rift to convergence in iberia. In: Quesada, C., Oliveira, J.T. (Eds.), The Geology of Iberia: A Geodynamic Approach, vol. 3. Springer Nature Switzerland, pp. 285–376. https://doi.org/10.1007/978-3-030-11295-0_7. The Alpine Cycle. Regional Geology Reviews.

McClay, K., Muñoz, J.A., García-Senz, J., 2004. Extensional salt tectonics in a contractional orogen: a newly identified tectonic event in the Spanish Pyrenees. Geology 32, 737–740.
Mencos, J., Carrera, N., Muñoz, J.A., 2015. Influence of rift basin geometry on the subsequent postrift sedimentation and basin inversion: the Organyà Basin and the Bóixols thrust sheet (south central Pyrenees). Tectonics 34, 1452–1474. https://doi.org/10.1002/2014tc003692.
Millán, H., Pueyo, E.L., Aurell, C., Luzón, A., Oliva-Urcía, B., Martínez-Peña, M., Pocoví, A., 2000. Actividad tectónica registrada en los depósitos terciarios del frente meridional del Pirineo central. Rev. Soc. Geol. Espana 13, 279–300.
Miró, J., Ferrer, O., Muñoz, J.A., Manastchal, G., 2023. Role of inheritance during tectonic inversion of a rift system in basement-involved to salt-decoupled transition: analogue modelling and application to the Pyrenean–Biscay system. Solid Earth 14, 425–445. https://doi.org/10.5194/se-14-425-2023.
Misch, P., 1934. Der Bau der mittleren Südpyrenäen. Abhandlungen der Gesellschaft der Wissenchaften zu Göttingen. Mathematisch-Physikalische Klasse 3 (12), 1597–1764. Spanish translation by J. Gómez de Llarena: "La estructura tectónica de la región central de los Pirineos meridionales". Publicaciones Extranjeras sobre Geología de España, 1943, 4, 7-180.
Mochales, T., Casas, A.M., Pueyo, E.L., Barnolas, A., 2012. Rotational velocity for oblique structures (BoltaNa anticline, Southern Pyrenees). J. Struct. Geol. 35, 2–16. https://doi.org/10.1016/j.jsg.2011.11.009.
Muñoz, J.A., 1992. Evolution of a continental collision belt: ECORS- Pyrenees crustal balanced section. In: McClay, K.R. (Ed.), Thrust Tectonics. Chapman and Hall, London, pp. 235–246.
Muñoz, J.A., 2002. The Pyrenees. In: Gibbons, W., Moreno, T. (Eds.), The Geology of Spain. The Geological Society of London, London, pp. 370–385.
Muñoz, J.A., Martínez, A., Vergés, J., 1986. Thrust sequences in the eastern Spanish Pyrenees. J. Struct. Geol. 8, 399–405.
Muñoz, J., Beamud, E., Fernández, O., Arbués, P., Dinarès-Turell, J., Poblet, J., 2013. The Ainsa Fold and thrust oblique zone of the central Pyrenees: kinematics of a curved contractional system from paleomagnetic and structural data. Tectonics 32, 1142–1175. https://doi.org/10.1002/tect.20070.
Muñoz, J.A., Mencos, J., Roca, E., Carrera, N., Gratacos, O., Ferrer, O., Fernández, O., 2018. The structure of the South-Central Pyrenean fold and thrust belt as constrained by subsurface data. Geol. Acta: Int. Earth Sci. J. 16, 439–460. https://doi.org/10.1344/geologicaacta2018.16.4.7.
Mutti, E., Séguret, M., Sgavetti, M., 1988. Sedimentation and defor- mation in the Tertiary sequences of the southern Pyrenees. AAPG Mediteranean Basins Conf. Nice, Field Trip Guideb. 7, 169.
Oliva-Urcía, B., Pueyo, E.L., 2007. Gradient of shortening and vertical-axis rotations in the Southern Pyrenees (Spain), insights from a synthesis of paleomagnetic data. Rev. Soc. Geol. Esp. 20 (1–2), 105–118.
Pla, O., Roca, E., Xie, H., Izquierdo-Llavall, E., Muñoz, J.A., Rowan, M.G., Ferrer, O., Gratacós, Ò., Yuan, N., Huang, S., 2019. Influence of syntectonic sedimentation and décollement rheology on the geometry and evolution of orogenic wedges: analog modeling of the kuqa fold-and-thrust belt (NW China). Tectonics 38, 2727–2755. https://doi.org/10.1029/2018tc005386.
Poblet, J., Muñoz, J.A., Travé, A., Serra-Kiel, J., 1998. Quantifying the kinematics of detachment folds using three-dimensional geometry: application to the Mediano anticline (Pyrenees, Spain). GSA Bulletin 110, 111–125. https://doi.org/10.1130/0016-7606(1998)110<0111:qtkodf>2.3.co;2.
Rodriguez-Pintó, A., Pueyo, E.L., Calvín, P., Sánchez, E., Ramajo, J., Casas, A.M., Ramón, M.J., Pocoví, A., Barnolas, A., Román, T., 2016. Rotational kinematics of a curved fold: the Balzes anticline (Southern Pyrenees). Tectonophysics 677–678, 171–189. https://doi.org/10.1016/j.tecto.2016.02.049.
Rowan, M.G., Vendeville, B.C., 2006. Foldbelts with early salt withdrawal and diapirism: physical model and examples from the northern Gulf of Mexico and the Flinders Ranges, Australia. Mar. Petrol. Geol. 23, 871–891. https://doi.org/10.1016/j.marpetgeo.2006.08.003.
Santolaria, P., Casas-Sainz, A.M., Soto, R., Casas, A., 2017. Gravity modelling to assess salt tectonics in the western end of the South Pyrenean Central Unit. J. Geol. Soc. 174, 269–288. https://doi.org/10.1144/jgs2016-027.
Santolaria, P., Ferrer, O., Rowan, M.G., Snidero, M., Carrera, N., Granado, P., Muñoz, J. A., Roca, E., Schneider, C.L., Piña, A., Zamora, G., 2021. Influence of preexisting salt diapirs during thrust wedge evolution and secondary welding: insights from analog modeling. J. Struct. Geol. 149, 104374 https://doi.org/10.1016/j.jsg.2021.104374.
Santolaria, P., Izquierdo-Lavall, E., Soto, R., Román-Berdiel, T., Casas-Sainz, A., 2024. Origin of oblique structures controlled by pre-1 tectonic thickness variations in frictional and salt-bearing fold-and-thrust belts: insights from analogue modelling. J. Struct. Geol. this volume.
Saura, E., Oró, L.A. i, Teixell, A., Vergés, J., 2016. Rising and falling diapirs, shifting depocenters, and flap overturning in the Cretaceous Sopeira and Sant Gervàs subbasins (Ribagorça Basin, southern Pyrenees). Tectonics 35, 638–662. https://doi.org/10.1002/2015tc004001.
Schellart, W.P., 2000. Shear test results for cohesion and friction coefficients for different granular materials: scaling implications for their usage in analogue modelling. Tectonophysics 324, 1–16. https://doi.org/10.1016/S0040-1951(00)00111-6.
Séguret, M., 1972. Étude tectonique des nappes et séries décollées de la partie centrale du versant sud des Pyrénées – caractère synsédimentaire, rôle de la compression et de la gravité, Série géologie structurale, vol. 2. Publications de l'Universite des Sciences et Techniques du Languedoc (USTELA), Montpellier, France, p. 155. France.
Sepehr, M., Cosgrove, J.W., 2004. Structural framework of the Zagros fold–thrust belt, Iran. Mar. Petrol. Geol. 21, 829–843. https://doi.org/10.1016/j.marpetgeo.2003.07.006.
Smeraglia, L., Fabbri, O., Choulet, F., 2021. Variation in structural styles within fold-and-thrust belts: insights from field mapping, cross-sections balancing, and 2D-kinematic modelling in the Jura mountains (Eastern France). J. Struct. Geol. 149, 104381 https://doi.org/10.1016/j.jsg.2021.104381.
Smit, J.H.W., Brun, J.P., Sokoutis, D., 2003. Deformation of brittle-ductile thrust wedges in experiments and nature. J. Geophys. Res. Solid Earth 108 (B10). https://doi.org/10.1029/2002jb002190.
Storti, F., Marin, R.S., Rossetti, F., Sainz, A.C., 2007. Evolution of experimental thrust wedges accreted from along-strike tapered, silicone-floored multilayers. J. Geol. Soc. 164, 73–85.
Sussman, A.J., Butler, R.F., Dinarès-Turell, J., Vergés, J., 2004. Vertical-axis rotation of a foreland fold and implications for orogenic curvature: an example from the Southern Pyrenees, Spain. Earth Planet Sci. Lett. 218, 435–449. https://doi.org/10.1016/s0012-821x(03)00644-7.
Teixell, A., Labaume, P., Ayarza, P., Espurt, N., Blanquat, M. de S., Lagabrielle, Y., 2018. Crustal structure and evolution of the Pyrenean-Cantabrian belt_ A review and new interpretations from recent concepts and data. Tectonophysics 724–725, 146–170. https://doi.org/10.1016/j.tecto.2018.01.009.
Vendeville, B.C., Pengcheng, T., Graveleau, F., Shaoying, H., Wang, X., 2017. How the presence of a salt décollement in the sedimentary cover influences the behavior of subsalt thrusts in fold-and-thrust belts. Bull. Soc. Geol. Fr. 188, 1–8. https://doi.org/10.1051/bsgf/2017202.
Vergés, J., 1993. Estudi geològic del vessant sud del Pirineu oriental i central. Evolució cinemàtica en 3D. PhD thesis. University of Barcelona.
Vergés, J., Muñoz, J., 1990. Thrust sequences in the southern central Pyrenees. Bull. Soc. Geol. Fr. 2, 265–271.
Vidal-Royo, O., Koyi, H.A., Muñoz, J.A., 2009. Formation of orogen-perpendicular thrusts due to mechanical contrasts in the basal décollement in the Central External Sierras (Southern Pyrenees, Spain). J. Struct. Geol. 31, 523–539. https://doi.org/10.1016/j.jsg.2009.03.011.
Vincent, S., 1999. The role of sediment supply in controlling alluvial architecture: an example from the Spanish Pyrenees. J. Geol. Soc. 156, 749–759.
Weil, A.B., Sussman, A.J., 2004. Classifying curved orogens based on timing relationships between structural development and vertical-axis rotations. In: Sussman, A.J., Weil, A.B. (Eds.), Orogenic Curvature: Integrating Paleomagnetic and Structural Analyses, vol. 383. Spec. Pap. Geol. Soc. Am, pp. 1–17.
Weil, A.B., Yonkee, A., Sussman, A., 2010. Reconstructing the kinematic evolution of curved mountain belts: a paleomagnetic study of Triassic red beds from the Wyoming salient, Sevier thrust belt. U.S.A. Geol. Soc. Am. Bullet. 122, 3–23. https://doi.org/10.1130/b26483.1.
Werf, I. van der, Schellart, W.P., Strak, V., Agtmaal, L. van, Blankendal, R., 2023. Analogue modelling of the Ainsa oblique zone in the southern central Pyrenees, Spain. J. Struct. Geol. 177, 104964 https://doi.org/10.1016/j.jsg.2023.104964.
Wu, Z., Yin, H., Wang, X., Zhao, B., Jia, D., 2014. Characteristics and deformation mechanism of salt-related structures in the western Kuqa depression, Tarim basin: insights from scaled sandbox modeling. Tectonophysics 612–613, 81–96. https://doi.org/10.1016/j.tecto.2013.11.040.